



Publication Year	2019
Acceptance in OA @INAF	2021-02-10T15:43:49Z
Title	The interstellar medium of dwarf galaxies: new insights from Machine Learning analysis of emission-line spectra
Authors	Ucci, G.; Ferrara, A.; Gallerani, S.; Pallottini, A.; CRESCI, GIOVANNI; et al.
DOI	10.1093/mnras/sty2894
Handle	http://hdl.handle.net/20.500.12386/30295
Journal	MONTHLY NOTICES OF THE ROYAL ASTRONOMICAL SOCIETY
Number	483

The interstellar medium of dwarf galaxies: new insights from Machine Learning analysis of emission-line spectra

G. Ucci¹,¹★ A. Ferrara,^{1,2} S. Gallerani,¹ A. Pallottini¹,^{1,3,4,5} G. Cresci,⁶ C. Kehrig,⁷ L. K. Hunt¹,⁶ J. M. Vilchez¹,⁷ and L. Vanzì⁸

¹*Scuola Normale Superiore, Piazza dei Cavalieri 7, I-56126 Pisa, Italy*

²*Kavli IPMU, The University of Tokyo, 5-1-5 Kashiwanoha, Kashiwa 277-8583, Japan*

³*Centro Fermi, Museo Storico della Fisica e Centro Studi e Ricerche ‘Enrico Fermi’, Piazza del Viminale 1, I-00184 Roma, Italy*

⁴*Cavendish Laboratory, University of Cambridge, 19 J. J. Thomson Ave, Cambridge CB3 0HE, UK*

⁵*Kavli Institute for Cosmology, University of Cambridge, Madingley Road, Cambridge CB3 0HA, UK*

⁶*INAF - Osservatorio Astrofisico di Arcetri, largo E. Fermi 5, I-50127 Firenze, Italy*

⁷*Instituto de Astrofísica de Andalucía, CSIC, Apartado de correos 3004, E-18080 Granada, Spain*

⁸*Department of Electrical Engineering and Centre of Astro Engineering, Pontificia Universidad Católica de Chile, Av. Vicuña Mackenna, 4860 Santiago, Chile*

Accepted 2018 October 23. Received 2018 October 8; in original form 2018 July 3

ABSTRACT

Dwarf galaxies are ideal laboratories to study the physics of the interstellar medium (ISM). Emission lines have been widely used to this aim. Retrieving the full information encoded in the spectra is therefore essential. This can be efficiently and reliably done using Machine Learning (ML) algorithms. Here, we apply the ML code GAME to MUSE (Multi Unit Spectroscopic Explorer) and PMAS (Potsdam Multi Aperture Spectrophotometer) integral field unit observations of two nearby blue compact galaxies: Henize 2-10 and IZw18. We derive spatially resolved maps of several key ISM physical properties. We find that both galaxies show a remarkably uniform metallicity distribution. Henize 2-10 is a star-forming-dominated galaxy, with a star formation rate (SFR) of about $1.2 M_{\odot} \text{ yr}^{-1}$. Henize 2-10 features dense and dusty (A_V up to 5–7 mag) star-forming central sites. We find IZw18 to be very metal-poor ($Z = 1/20 Z_{\odot}$). IZw18 has a strong interstellar radiation field, with a large ionization parameter. We also use models of PopIII stars spectral energy distribution as a possible ionizing source for the He II $\lambda 4686$ emission detected in the IZw18 NW component. We find that PopIII stars could provide a significant contribution to the line intensity. The upper limit to the PopIII star formation is 52 per cent of the total IZw18 SFR.

Key words: galaxies: abundances – galaxies: evolution – galaxies: individual: He 2-10 – galaxies: individual: IZw18 – galaxies: ISM – galaxies: star formation.

1 INTRODUCTION

Emission lines in the spectra of galaxies contain a huge amount of information on the physical properties of their interstellar medium (ISM). The ISM of local blue compact galaxies (BCGs), a subclass of dwarf galaxies, represents a particularly interesting case of study. In fact, since BCGs are low-metallicity, compact, star-forming systems, they are thought to represent local analogues of early galaxies (Lequeux et al. 1979; Garland et al. 2015) that will become soon observable in greater detail with forthcoming instruments (e.g. JWST). Given their small distances, local BCGs can be studied at much higher spatial resolution with respect to high-redshift galaxies. Thus, ISM studies of local BCGs can be used as

benchmarks for understanding the structure, formation, and evolution of high-redshift galaxies. The concept of BCG was firstly introduced by Zwicky (1965) to refer to ‘quasi-stellar galaxies’, namely galaxies with pure emission-line spectra, initially barely distinguishable from stars (Arp 1965). Since the spectra of BCGs resemble galactic H II regions (Haro 1956; Zwicky 1966; Markarian 1967), these galaxies are also called H II galaxies (Markarian 1967; Sargent & Searle 1970; Melnick, Terlevich & Eggleton 1985; Hazard 1986; Terlevich et al. 1991). This is the case of Henize 2-10 (Corbin, Korista & Vacca 1993), a Wolf–Rayet starburst galaxy with a central radio source, a metallicity of $12 + \log(\text{O}/\text{H}) = 8.55 \pm 0.02$ (Esteban et al. 2014), intense star formation rate ($\text{SFR} \sim 1.9 M_{\odot} \text{ yr}^{-1}$; see Reines et al. 2011), and the possible presence of an active massive black hole (Reines et al. 2016, but see also Cresci et al. 2017).

* E-mail: graziano.ucci@sns.it

BCGs have different physical properties compared to other varieties of star-forming galaxies (Arp 1965, Zwicky 1966). In fact, their star formation occurs in short bursts, separated by long ($\sim 10^7$ yr) quiescent periods (Sargent & Searle 1970; Searle & Sargent 1972; Searle, Sargent & Bagnuolo 1973; Kunth & Östlin 2000) resulting in young stellar populations (with commonly accepted indications of older underlying population; Tolstoy, Hill & Tosi 2009), and a small amount of dust. Very low metallicity values have been indeed measured in several BCGs: IZw18 [$12 + \log(\text{O}/\text{H}) = 7.17 \pm 0.04$; Searle & Sargent 1972; Dufour, Garnett & Shields 1988; Skillman & Kennicutt 1993; the starburst galaxy SBS 0335-052W (Izotov et al. 1990, 1997; Izotov, Thuan & Guseva 2005; Izotov et al. 2009) with $12 + \log(\text{O}/\text{H}) = 7.13 \pm 0.02$ (Izotov et al. 2009); the irregular galaxy DDO 68 ($12 + \log(\text{O}/\text{H}) = 7.21 \pm 0.03$; Pustilnik, Kniazev & Pramskij 2005; Berg et al. 2012); the low-luminosity dwarf Leo P [$12 + \log(\text{O}/\text{H}) = 7.17 \pm 0.04$, Skillman et al. 2013; McQuinn et al. 2015; AGC 198691, the most metal-poor galaxy known in the local Universe [$12 + \log(\text{O}/\text{H}) = 7.02 \pm 0.03$; Hirschauer et al. 2016].

Most of the results reported above have been obtained by adopting diagnostics based on emission-line ratios. An alternative, promising approach relies on Machine Learning (ML) techniques (Ucci et al. 2017, 2018, hereafter U17 and U18). In this work, we study the ISM physical properties of Henize 2-10 and IZw18 by processing their integral field unit (IFU) observations with the ML code GAME (GALaxy Machine learning for Emission lines U17, U18). The advantage of this code relies on the fact that it is possible to infer simultaneously several ISM physical properties by using all the information in the spectra. The purpose of this work is to apply GAME in the case of two well-studied examples of local BCGs in view of future applications, especially at high redshifts.

The paper is organized as follows: in Section 2, we summarize the main features of the GAME code; in Sections 3 and 4, we present the results for Henize 2-10 and IZw18, respectively; in Section 5, we discuss and summarize the main results of this study.

2 INFERRING ISM PHYSICAL PROPERTIES

GAME is an ML code that infers the ISM physical properties by analyzing the emission-line intensities in a galaxy spectrum (for the complete description see U17, U18). The code is based on a supervised ML algorithm, and it is trained with a library of 100 000 synthetic spectra spanning many different ISM phases, including H II (ionized) regions, PDRs, and neutral regions (U17, U18). The library of synthetic spectra is generated by using the photoionization code CLOUDY v13.03 (Ferland et al. 2013) by varying the total (i.e. H I + H II + H₂) gas density (n), total column density (N_{H}), ionization parameter¹ (U), and metallicity² (Z); the library contains PopII and PopIII stellar populations (see U18). The emission-line library is then processed in order to account for noise in the observations (U18). Given a set of input lines in a spectrum, the ML performs a training on the library, then evaluates the line intensities to give a determination of the physical properties; each physical property is determined by the AdaBoost ML algorithm separately and independently (U17). The errors on the input emission-line intensities

and the uncertainties on the physical properties determinations have been taken into account and they have been included in the analysis (U18).

It is important to notice that GAME does not use a pre-selected subset of emission-line ratios (i.e. [N II]/H α , R₂₃), but rather reconstructs the ISM properties of galaxies exploiting all the lines available in the input, including the faint ones. As showed in U18, the accuracy of the determination of the physical properties improves with an increasing number of emission lines.

The physical properties directly inferred by GAME in this work are: gas density (n), column density (N_{H}), ionization parameter (U), metallicity (Z), far-ultraviolet (FUV, 6–13.6 eV) flux (G),³ visual extinction (A_V). Starting from these properties, it is possible to derive information also on the star formation surface density (Σ_{SFR}), and the gas mass surface density (Σ_{gas}), as detailed below. We can use N_{H} maps to obtain an estimate of the total gas mass contained in each spaxel of the map:

$$M = \mu m_{\text{H}} N_{\text{H}} A_{\text{spax}}, \quad (1)$$

where μ is the mean molecular weight (in the following we assume $\mu = 1.4$), m_{H} is the hydrogen atom mass, and A_{spax} is the spaxel area. The gas mass surface density is then

$$\Sigma_{\text{gas}} = \mu m_{\text{H}} N_{\text{H}}. \quad (2)$$

Using these quantities, we can also infer the SFR surface density (Σ_{SFR}), by assuming a Schmidt–Kennicutt relation (Schmidt 1959; Kennicutt 1998; Krumholz, Dekel & McKee 2012):

$$\Sigma_{\text{SFR}} = \eta \frac{\Sigma_{\text{gas}}}{t_{\text{sf}}}, \quad (3)$$

where η is the star formation efficiency and t_{sf} is the star formation time scale. As shown by Krumholz et al. (2012), the relation is well fitted in a variety of environments by using $t_{\text{sf}} = t_{\text{ff}}$, where t_{ff} is the gas free-fall time, and $\eta = 0.015$. Thus, we can write equation (3) in terms of quantities directly derived from GAME (i.e. n and N_{H}):

$$\Sigma_{\text{SFR}} = 0.015 m_{\text{H}}^{3/2} N_{\text{H}} \sqrt{\frac{32 G n}{3 \pi}}. \quad (4)$$

Alternatively, it is also possible to derive the SFR from the H α line intensity after correcting for the dust extinction, using specific calibrators (Kennicutt 1998; Calzetti et al. 2007; Kennicutt & Evans 2012). In Section 3.1.5, we will show a comparison between the SFR estimated via equation (4) and the calibration from Calzetti (2008) with different dust extinction laws. We now apply GAME to the study of two BCGs, Henize 2-10 and IZw18.

3 HENIZE 2-10

The blue compact local galaxy Henize 2-10 (hereafter He 2-10) can be considered as a prototype of an H II (Allen, Wright & Goss 1976) Wolf–Rayet (Dodorico, Rosa & Wampler 1983; Kawara et al. 1987; Conti 1991; Vacca & Conti 1992) starburst galaxy. It is located at a distance of 8.23 Mpc (Tully et al. 2013) with a corresponding angular scale of 40 pc arcsec, and its core has an optical extent less than 1 kpc. He 2-10 has been extensively studied both in the optical and in the infrared wavelength ranges (Vanzi & Rieke 1997; Vacca, Johnson & Conti 2002; Engelbracht et al. 2005), up to the submillimetre (Bayet et al. 2004; Johnson et al. 2017). It has a

¹In this work, we adopted the following definition for the ionization parameter: $U = Q(H)/(4\pi R_S^2 n c)$, where $Q(H)$ is the ionizing photon flux, c is the speed of light, and R_S is the Strömgren radius.

²In the library, we assumed fixed solar abundance ratios for all the elements (U18).

³For a given library spectrum G , n , and U are directly related, but they are determined independently by the ML algorithm, as explained in the text.

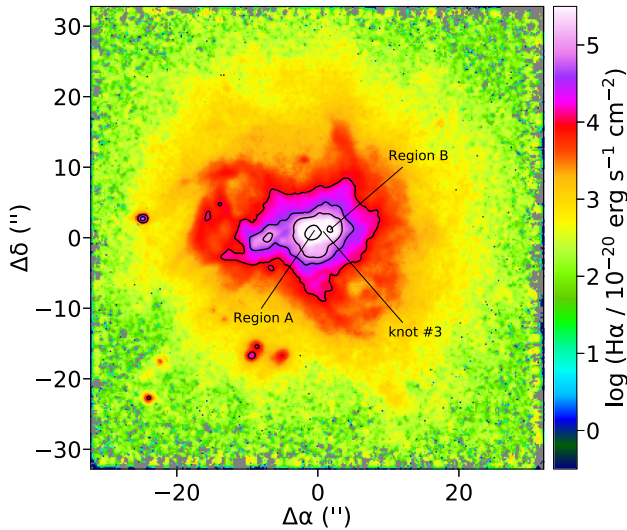


Figure 1. $H\alpha$ image of He 2-10 (Cresci et al. 2017). Black lines show the contours of the $H\alpha$ emission (80, 10, 4, and 1 in units of $10^{-16} \text{ erg s}^{-1} \text{ cm}^{-2}$). The $H\alpha$ contour levels are the same as in Cresci et al. (2017) in order to be able to directly compare their figures. Shown are the two regions A and B where the $H\alpha$ flux peaks. We also show the radio source designated by Johnson & Kobulnicky (2003) as knot #3. The field of view of the image is $(64 \text{ arcsec})^2$ corresponding to a physical size of $(2.56 \text{ kpc})^2$.

stellar mass of $(10 \pm 3) \times 10^9 M_{\odot}$ (Reines et al. 2011; Nguyen et al. 2014). The estimated SFR is $\sim 1.9 M_{\odot} \text{ yr}^{-1}$ (Reines et al. 2011), as revealed by classical indicators such as the $H\alpha$ (Méndez et al. 1999) and the $24 \mu\text{m}$ flux (Engelbracht et al. 2005). In Fig. 1, we show the $H\alpha$ image of He 2-10. The bulk of the $H\alpha$ emission is located in two central emitting regions (hereafter Region A and B) separated by $\sim 2 \text{ arcsec}$ ($\sim 80 \text{ pc}$).

An unresolved non-thermal nuclear source has been found in the nucleus of He 2-10 (Kobulnicky & Johnson 1999; Johnson & Kobulnicky 2003). This source (designated as knot #3) is located between Regions A and B in Fig. 1. Reines et al. (2011) linked this source to the presence of a compact X-ray emission detected with Chandra observations (Kobulnicky & Martin 2010). The size of this emitting region has been constrained to be $< 1 \text{ pc} \times 3 \text{ pc}$ (Reines & Deller 2012) and recently associated with the presence of a weakly accreting supermassive black hole having mass $\log(M/M_{\odot}) \sim 6.3$ (Reines et al. 2016). The origin of the X-ray emission in He 2-10 is still debated (Cresci et al. 2017). We further discuss this point in Appendix A where we show that on scales larger than $\sim 4 \text{ pc}$ from the centre, the radiation field is dominated by stars.

3.1 ISM physical properties in He 2-10

In this section, we present a systematic overview of the ISM physical properties in He 2-10, inferred by applying GAME (U17, U18) to MUSE (Multi Unit Spectroscopic Explorer; Bacon et al. 2010) optical integral field observations taken from Cresci et al. (2017). We have a total of $321 \times 328 = 105\,288$ spaxels with a spatial sampling of $0.2 \text{ arcsec} \times 0.2 \text{ arcsec}$. The spectral resolution (i.e. $R = \lambda/\Delta\lambda$) goes from 1750 at 4650 \AA to 3750 at 9300 \AA (Cresci et al. 2015, 2017). The emission lines used as input for GAME are reported in Table 1 along with the fraction of spaxels with a detected and fitted line, having $\text{SNR} > 3$. For details on the line fitting procedure, we refer the reader to Cresci et al. (2017).

Table 1. Emission lines and wavelengths used to analyse the galaxy He 2-10. The third column reports the fraction of spaxels with a detected and fitted line, having $\text{SNR} > 3$.

Line	Wavelength (\AA)	Fraction of spaxels (%)
$H\beta$	4861	20
[O III]	5007	15
He I	5876	3
[O I]	6300	2
$H\alpha$	6563	36
[N II]	6584	18
He I	6678	1
[S II]	6717	15
[S II]	6731	11
[S III]	9069	2

The resulting maps [median radial profiles⁴ centered on $(\Delta\alpha, \Delta\delta) = (0,0)$] of the inferred physical properties are reported in Figs 2 and 5 (Figs 3 and 6). As observations outside the centre of the galaxy become noisy, we selected only the lines with $\text{SNR} > 3$ (see Table 1). Then, we analyzed the spaxels with at least six lines satisfying this condition (see discussion in appendix D of U18). These spaxels are the ones plotted in each panel of Figs 2 and 5. In Appendix B, we also report the uncertainties on the physical properties computed with GAME on all the spaxels visualized.

3.1.1 Gas density

The gas density map (n) in the upper left panel of Fig. 2 shows that the highest density is reached close to Regions A and B, where $\log(n/\text{cm}^{-3}) \sim 3.3$. For distances $d \gtrsim 5 \text{ arcsec}$ ($\gtrsim 200 \text{ pc}$) from the centre, the median density radial profile in the galaxy decreases until a distance of $\sim 350 \text{ pc}$ around a value of $\log(n/\text{cm}^{-3}) \sim 0.5$ (see Fig. 3). The upper-right panel of Fig. 2 shows that column densities in the He 2-10 central region (i.e. within 10 arcsec from the centre) vary from $\sim 10^{20} \text{ cm}^{-2}$ up to $\sim 3 \times 10^{22} \text{ cm}^{-2}$, consistently with results found in literature (Baas, Israel & Koornneef 1994; Kobulnicky et al. 1995; Meier et al. 2001; Santangelo et al. 2009; Cresci et al. 2017).

The left-hand panel of Fig. 4 shows the map of the effective scale height of the disc, defined as $H = N_H/n$. In the right-hand panel, we zoom in the central region [$5 \text{ arcsec} \times 5 \text{ arcsec}$, i.e. $200 \times 200 \text{ pc}^2$], where the uncertainties are smaller (see Fig. B1 in Appendix B). In the central region, we find a relatively small height of the disc, i.e. $-0.5 \lesssim \log(H/\text{pc}) \lesssim 1.5$ ($0.3 \lesssim H/\text{pc} \lesssim 30$). This is the typical dimension of giant molecular clouds (GMCs) that we are resolving in the centre of the galaxy. Regions A and B, with their high values of densities and metallicities, and given also the high $H\alpha$ and FUV flux G , can be identified as the sites of intense star formation.

3.1.2 Metallicity

The metallicity map and the corresponding radial profile are reported in the central left-hand panels of Figs 2 and 3, respectively. We find that Regions A and B ($d \lesssim 4 \text{ arcsec}$) are characterized by supersolar values [$\log(Z/Z_{\odot}) \sim 0.2-0.3$], while at larger distances

⁴Because the physical properties distributions in the inferred maps are relatively spread, we preferred to use the median instead of the average in order to prevent an increase of the radial profiles purely driven by the presence of few high values.

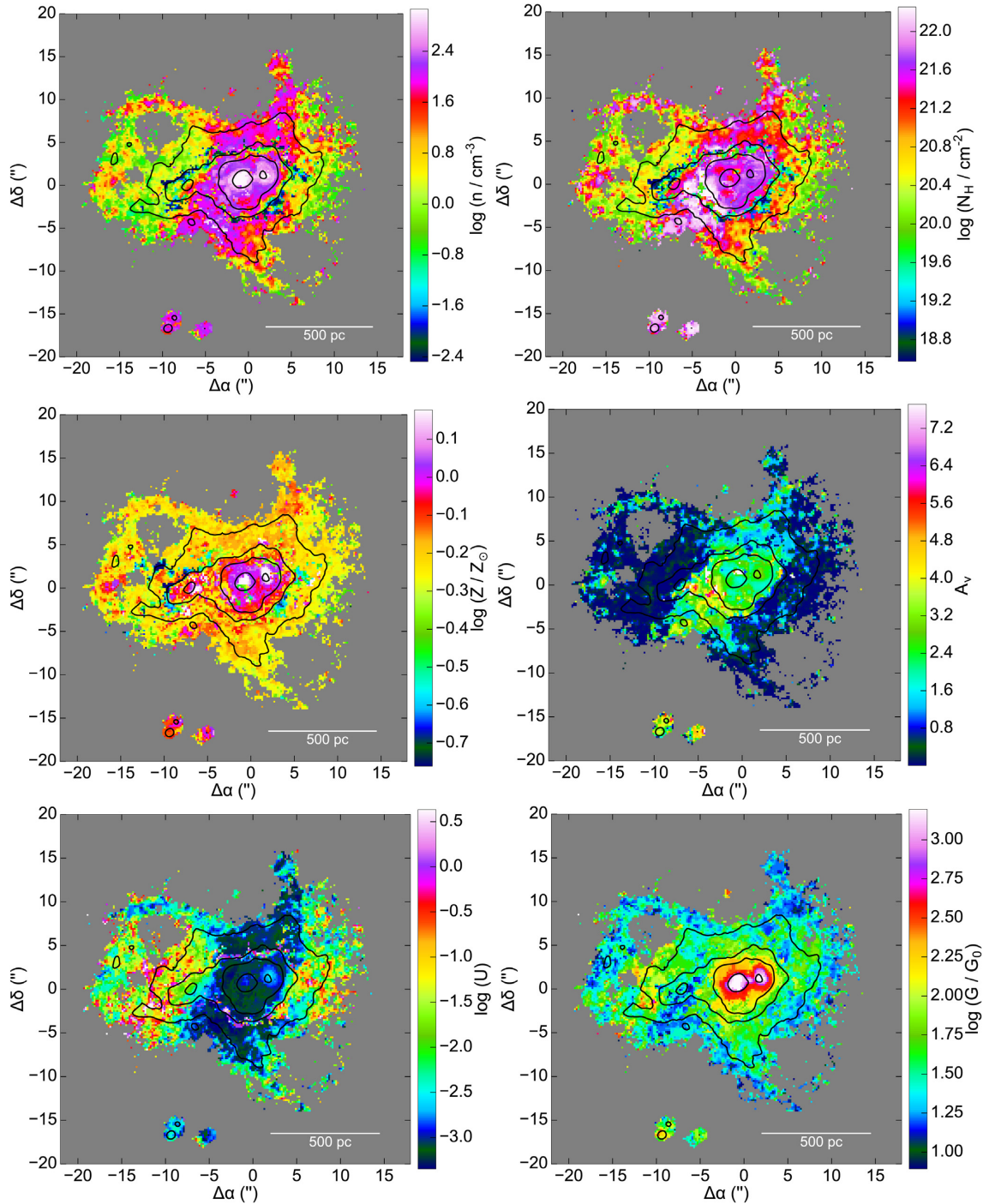


Figure 2. Maps of the ISM physical properties inferred for the local galaxy He 2-10 using the code GAME (U17; U18): density (n), column density (N_{H}), metallicity (Z), visual extinction (A_V), ionization parameter (U), and the FUV flux in Habing units (G/G_0). As in Fig. 1, black lines show the contours of the H α emission line (80, 10, 4, and 1 in units of $10^{-16} \text{ erg s}^{-1} \text{ cm}^{-2}$).

($4 \text{ arcsec} \lesssim d \lesssim 10 \text{ arcsec}$) the metallicity is slightly subsolar [i.e. $\log(Z/Z_{\odot}) \sim -0.15$] and remarkably uniform (within a factor of ~ 2). The obtained average metallicity [$12 + \log(\text{O}/\text{H}) \sim 8.6$] is the one expected from the mass–metallicity relation for a galaxy with a stellar mass of $M_{*} \sim 10^{10} M_{\odot}$, i.e. $12 + \log(\text{O}/\text{H}) \sim 8.7$ (Sánchez et al. 2017).

We also compare our results with the radial profiles of Cresci et al. (2017) who adopted the D16 (Dopita et al. 2016) and the O3N2 (Curti et al. 2017) calibrators (Fig. 3). The metallicities ob-

tained with GAME are between the results obtained through the O3N2 and D16 calibrators. In particular, in Fig. 7 we compare the distributions of the derived metallicity values inferred through the three different methods. The distribution obtained by GAME covers the same values inferred with the O3N2 and D16 methods, but spans a larger range [i.e. $-1.0 \lesssim \log(Z/Z_{\odot}) \lesssim 0.3$]. The standard deviations of the metallicity values inferred with the three approaches are, respectively: $\sigma(\text{GAME}) \sim 0.13$, $\sigma(\text{O3N2}) \sim 0.06$, $\sigma(\text{D16}) \sim 0.10$. The difference in the results obtained between this work and

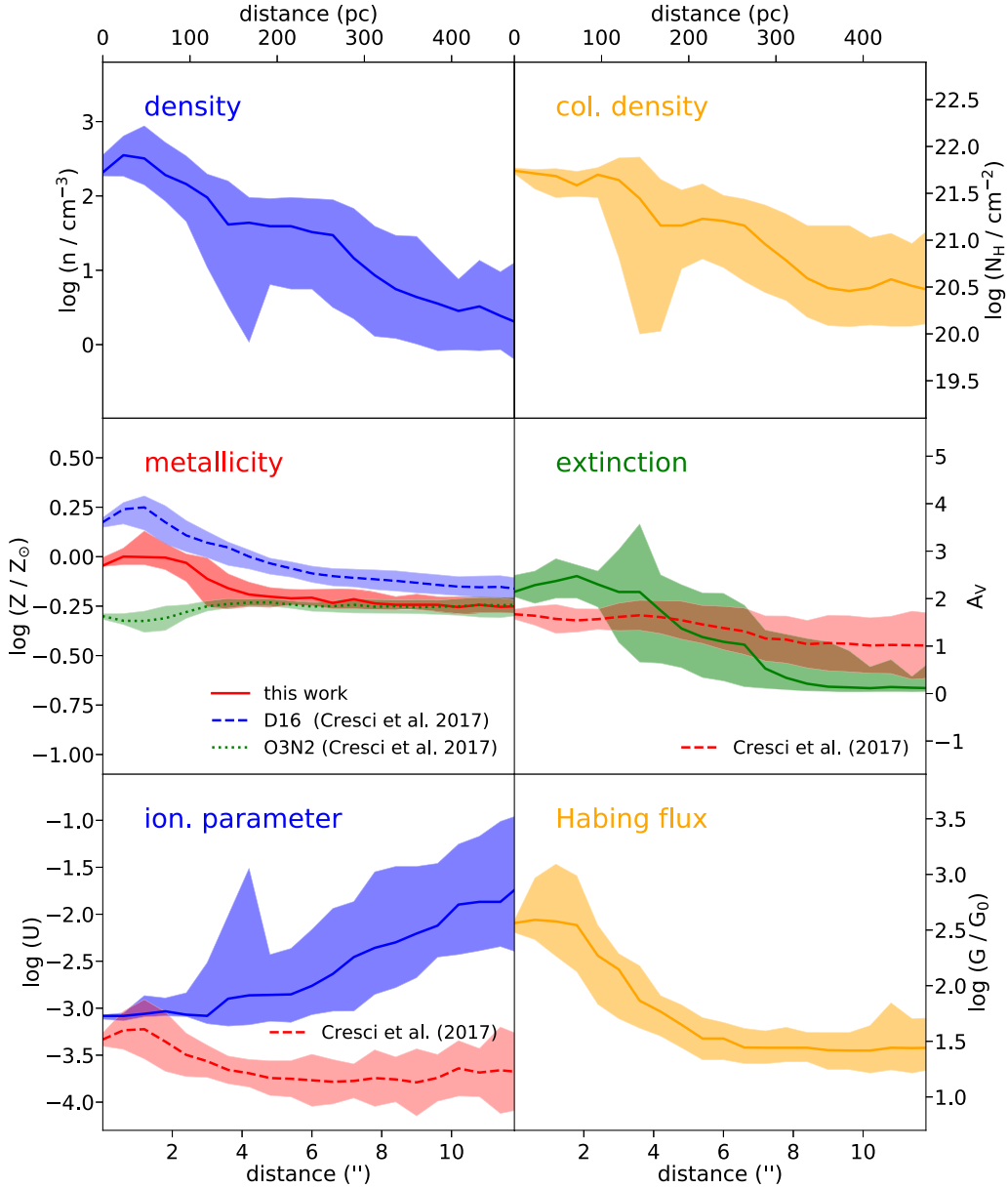


Figure 3. Median radial profiles (median of the inferred physical property values in annular bins of 0.6 arcsec) of the He 2-10 ISM physical properties obtained from the maps shown in Fig. 2, centered on $(\Delta\alpha, \Delta\delta) = (0,0)$. Upper and lower shaded regions denote, respectively, the second and third quartiles. For metallicity, extinction, and ionization parameter, we also report the radial profiles as inferred by Cresci et al. (2017).

Cresci et al. (2017) can be ascribed to the fact that while the O3N2 and D16 diagnostics account for ionized regions only, the GAME results are based on a library spanning several phases of the ISM (U17, U18). In fact, the physical properties are inferred taking into account not only ionized gas constraints (see Table 1), but also lines coming from neutral (i.e. [O I]) and partially neutral regions (i.e. [S II]). In order to test this hypothesis, we have repeated the analysis removing the [O I] and [S II] lines, and we have checked whether the metallicity measurements are affected. In Fig. 8, we report the metallicity inferred with GAME using two different sets of input emission lines: one with all the input lines reported in Table 1 (left-hand panel), and one using only purely ionized input lines (right-hand panel), i.e. removing the [O I] and [S II] lines. In Fig. 9, we show the median radial profiles of the maps reported in Fig. 8, compared with the previous estimates by Cresci et al. (2017).

It is evident that the metallicity values inferred from ionized lines only (especially in the central region, $d \lesssim 5$ arcsec) are lower than the ones obtained using the full set of input emission lines (i.e. the one that contains also neutral and partially neutral emission lines).

3.1.3 Dust extinction

In Fig. 2, we show the map of the visual extinction A_V . In the central region of the galaxy (i.e. $d \lesssim 5$ arcsec) A_V ranges between 1 and 5 mag while in the outer regions (i.e. $d \gtrsim 8$ arcsec), the A_V median radial profile flattens to ~ 0.1 mag (see Fig. 3), although with a large dispersion.

Vacca & Conti (1992) measured $E(B - V) = 0.54$ (corresponding to $A_V = 1.7$ mag, assuming $R_V = 3.1$) from the Balmer decrement in

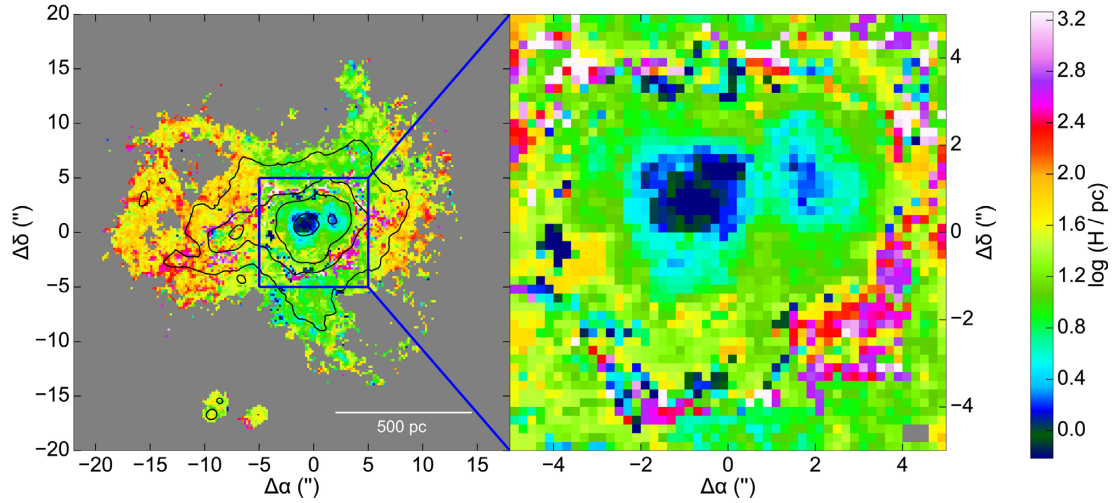


Figure 4. Left panel: ‘effective’ scale height defined as $H = N_H/n$. As in Fig. 1, black lines show the contours of the $H\alpha$ emission line (80, 10, 4, and 1 in units of $10^{-16} \text{ erg s}^{-1} \text{ cm}^{-2}$). Right-hand panel: zoom on the blue box.

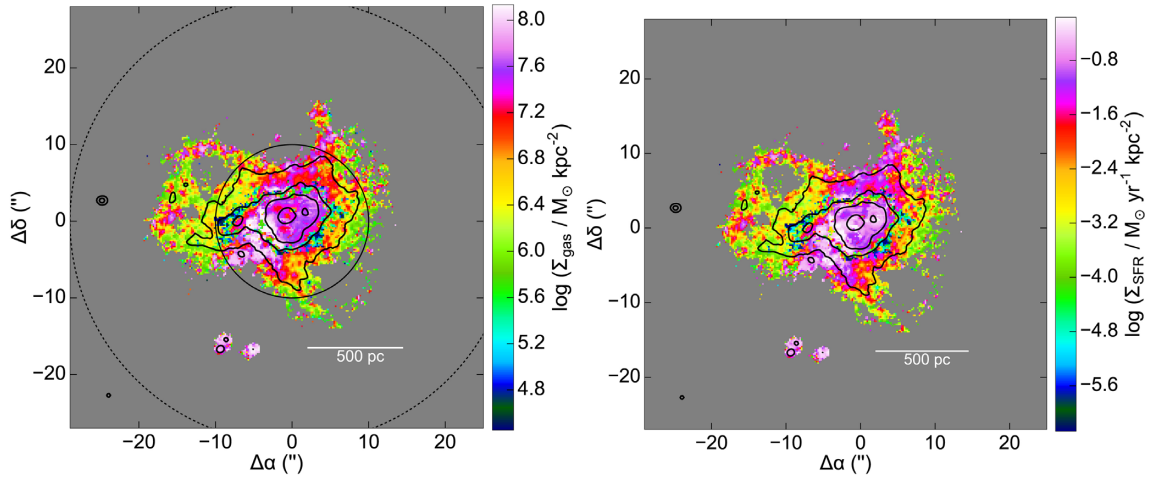


Figure 5. Gas mass surface density (Σ_{gas} , left-hand panel) and star formation surface density (Σ_{SFR} , right-hand panel) for the local galaxy He 2-10. As in Fig. 1, black lines show the contours of the $H\alpha$ emission line (80, 10, 4, and 1 in units of $10^{-16} \text{ erg s}^{-1} \text{ cm}^{-2}$). Inner and outer black circles denote the areas covered by the CO observations of Vanzi et al. (2009) and Kobulnicky et al. (1995), respectively (see the text for details).

optical slit spectroscopy. Cresci et al. (2017) obtained from optical lines $A_V \sim 2.3$ in Region B. Cabanac, Vanzi & Sauvage (2005) found $A_V = 1.25$ ($A_V = 10.5$) over an aperture of $2.4 \text{ arcsec} \times 15.6 \text{ arcsec}$ centered on the nucleus from the $H\alpha/\text{Br}\gamma$ ($\text{Br}\gamma/\text{Br}10$) ratio (see also Kawara, Nishida & Phillips 1989). From the $\text{Br}12/\text{Br}\gamma$ ratio, Cresci et al. (2010) obtained $A_V = 1.5\text{--}12 \text{ mag}$ in a region within $2\text{--}3 \text{ arcsec}$ from the centre. The inferred extinction found in literature from IR observations is higher with respect to the A_V estimated from the optical wavelength range. Since the central region of He 2-10 is a complex system characterized by the presence of absorbing material (i.e. gas and dust) mixed with emitting sources (Martín-Hernández et al. 2006), classic diagnostics based on optical lines do not allow A_V measurements into dust-embedded star-forming regions, as IR data do.

Fig. 2 shows that A_V mildly correlates with n , as quantified in Fig. 13 with a correlation coefficient $C = 0.64$. In the star-forming Regions A and B, we obtain $A_V \gtrsim 2\text{--}3 \text{ mag}$. The visual extinction reaches a peak in the SW part centered at $(\Delta\alpha, \Delta\delta) = (-4, -3)$, at $d \sim 4 \text{ arcsec}$ from the centre, where there is a region highly

correlated with high column densities ($N_H \gtrsim 10^{22} \text{ cm}^{-2}$). It is a region with $\Sigma_{\text{gas}} > 10^8 \text{ M}_\odot \text{ kpc}^{-2}$ and where most of the gas mass is located (e.g. Fig. 5), and already associated in Cresci et al. (2017) with an accreting cloud detected in CO observations.

3.1.4 Interstellar radiation field

We characterize the radiation field of He 2-10 in terms of the FUV flux G and the ionization parameter U , whose maps are shown in the bottom right and left panel of Fig. 2, respectively. From the median radial profile, the FUV flux in Habing units⁵ is $G/G_0 \sim 10^3$ in the centre of the galaxy (in correspondence of the highly star-forming Regions A and B), while at larger distances (i.e. $d \gtrsim 4 \text{ arcsec}$) it flattens around $G/G_0 \sim 10^{1.5}$. For what concerns the ionization parameter, $U \sim 10^{-3}$ in the central regions ($d \lesssim 4 \text{ arcsec}$), while at

⁵ $G_0 = 1.6 \times 10^{-3} \text{ erg s}^{-1} \text{ cm}^{-2}$ (Habing 1968).

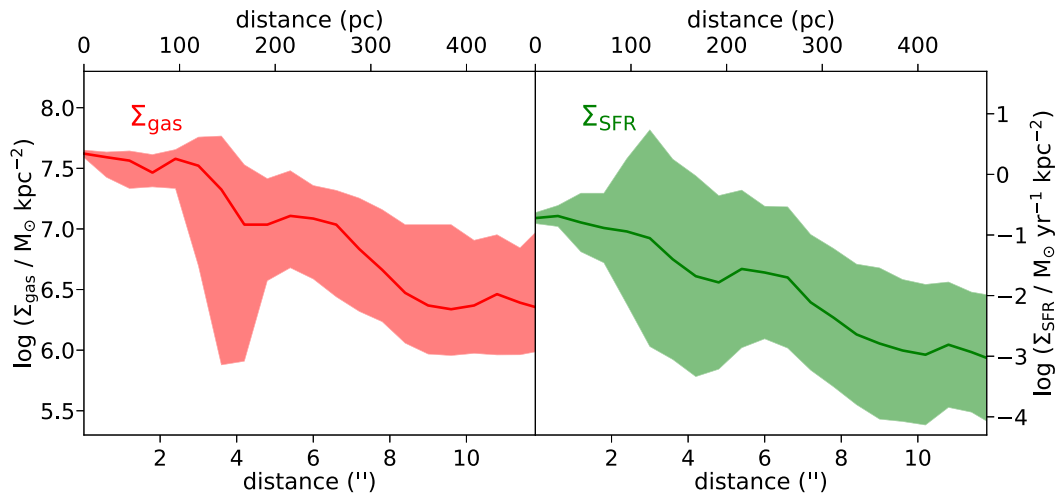


Figure 6. Median radial profiles (median of the inferred physical property values in annular bins of 0.6 arcsec) of He 2-10 Σ_{gas} and Σ_{SFR} (left- and right-hand panel, respectively) obtained from the maps shown in Fig. 5, and centered on $(\Delta\alpha, \Delta\delta) = (0,0)$. Upper and lower shaded regions denote, respectively, the second and third quartiles.

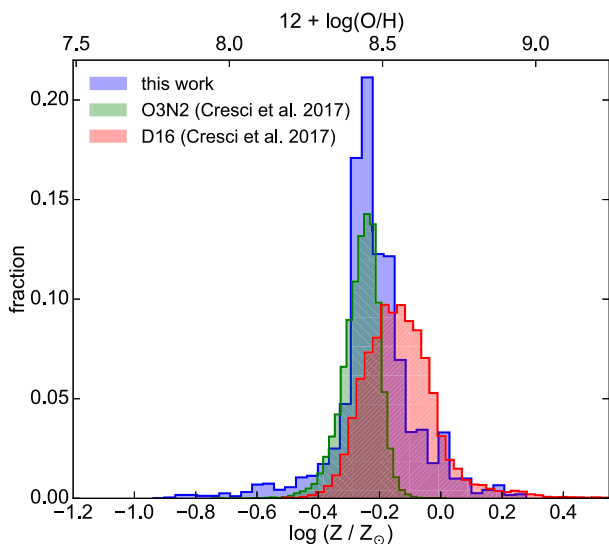


Figure 7. Distributions of the He 2-10 metallicity (central-left panel of Fig. 2). The blue shaded histogram reports the inferred values for the metallicity obtained in this work. The green and red shaded regions show the results obtained by Cresci et al. (2017) using the *O3N2* line ratio and the diagnostic by Dopita et al. (2016, *D16*), respectively.

larger distances $U \sim 10^{-1.5}$. Our results are consistent with the ones reported by Cresci et al. (2017) in the inner region of the galaxy while, at $d \gtrsim 2$ arcsec, GAME infers U values up to two orders of magnitude larger.⁶ In what follows, we analyse the physical origin of our findings.

⁶In the U map, we inferred values of the ionization parameter up to $\sim 10^{1.5}$, about 0.5–1.0 dex higher than the most extreme values found in the literature. However, the spaxels with these extreme values [i.e. $\log(U) > 1$] are found to be $\lesssim 5$ per cent of the total number and highly correlated with low-density regions. For further discussion see also Section 4.1.4.

The U profile depends on G and n according to the following relation⁷: $G/G_0 \sim 10^3 U n$. In Fig. 10, we compare the radial median profile of U (blue line/shaded region) with the one of $10^{-3} G/G_0 \sim n^{-1}$ (red line/shaded region), where U , G , and n are the values inferred by GAME independently. This figure shows that the expected physical trend is correctly recovered by the ML algorithm. At small distances ($d < 4$ arcsec), large values of the FUV flux $G/G_0 \sim 10^3$ are compensated by much larger values of the gas density ($n \sim 10^3 \text{ cm}^{-3}$), thus providing a small value of U ($\sim 10^{-3}$). Vice versa, at larger distances, the strong decrease of the gas density [$\log(n/\text{cm}^{-3}) \sim 0$, because of the strong anticorrelation with U , see Fig. 13] and the flattening of the FUV flux at the value $G/G_0 \sim 10^{1.5}$, combine into a large U value ($\gtrsim 10^{-2}$).

Cresci et al. (2017) used the line ratio $[\text{S III}]/[\text{S II}]$ to derive U , using the calibrations of Kewley & Dopita (2002). Our results are consistent with their findings only within few arcsec (~ 2 arcsec) from the centre of the galaxy, while our U values are larger in the outer regions. However, note that the U determination has large typical uncertainties. Thus, the U determination cannot be considered reliable in the outer region. The poor determination of U with respect to the other variables from GAME has been already discussed in U17. However, the discrepancy between our findings and the results from Cresci et al. (2017, see Fig. 3), following what we demonstrated in Section 3.1.2, could be ascribed to the fact that we used the full set of input emission lines available with no assumptions about the underlying emitting phase (i.e. without assuming emitting H II regions only). As evident from Fig. 12 (see also Fig. 11), the difference between the radial profiles assuming only ionized lines, reduces to ~ 0.5 dex (i.e. a factor of 3). If we assume instead the full set of available lines, at large radii ($d \gtrsim 9$ arcsec), the difference is $\gtrsim 1$ dex.

⁷The ratio between the number of FUV photons ($\propto G$) and the number of ionizing photons ($\propto U n$) depends on the shape of the stellar spectra that constitutes the GAME library that, in its turn, depends on the stellar metallicity. Given the almost flat metallicity radial profile, this ratio is not expected to vary along the disc of the galaxy.

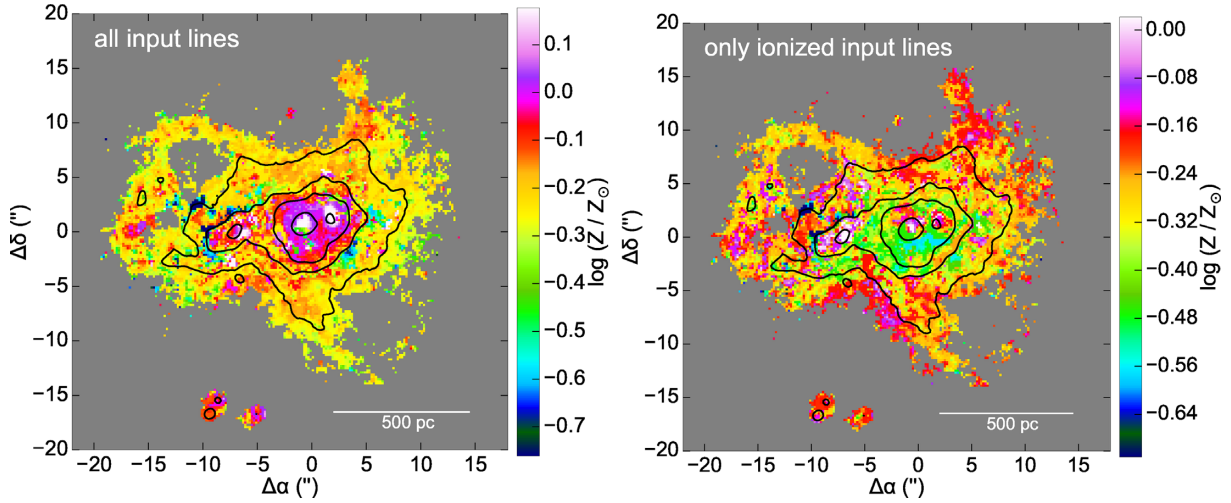


Figure 8. Left-hand panel: map of the ISM metallicity (Z) inferred for He 2-10 using all the input lines reported in Table 1. Right-hand panel: map of Z inferred for He 2-10 using only the ionized input lines reported in Table 1 (i.e. excluding the [O I] and [S II] lines). As in Fig. 1, black lines show the contours of the $H\alpha$ emission line (80, 10, 4, and 1 in units of 10^{-16} erg s^{-1} cm^{-2}).

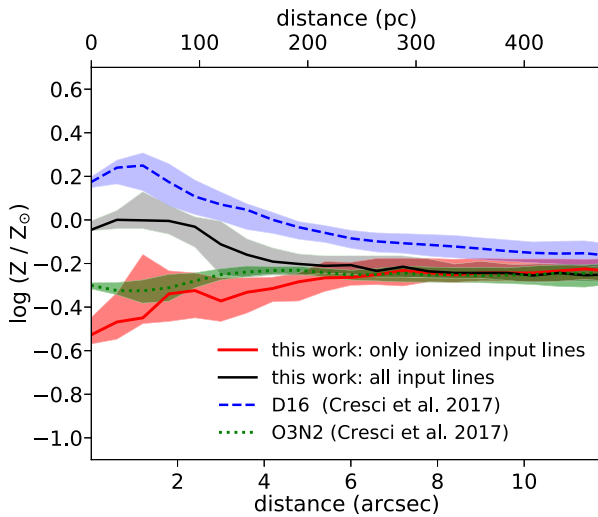


Figure 9. Median radial profiles (median of the inferred physical property values in annular bins of 0.6 arcsec) of the He 2-10 metallicity (Z) obtained from the maps shown in Fig. 8, centered on $(\Delta\alpha, \Delta\delta) = (0,0)$. Upper and lower shaded regions denote, respectively, the second and third quartiles. We also report the radial profiles as inferred by Cresci et al. (2017).

3.1.5 Gas mass and SFR surface density

We computed the gas mass surface density Σ_{gas} (see equation 2) by considering the spaxel area $A_{\text{spax}} = 64 \text{ pc}^2$.

Kobulnicky et al. (1995) estimated a molecular (atomic) hydrogen mass of $1.6 \pm 0.1 \times 10^8$ ($1.9 \pm 0.1 \times 10^8$) M_{\odot} from CO(1-0) and CO(2-1) detections. More recent observations based on CO(3-2) emission (Vanzi et al. 2009) provide a molecular mass of $1.4 \times 10^7 M_{\odot}$. In Fig. 5, the solid and dashed lines correspond to the sizes of the regions covered by the CO observations of Kobulnicky et al. (1995, a radius of ~ 23 arcsec) and Vanzi et al. (2009, a radius of ~ 10 arcsec), respectively. By summing up the contribution from spaxels within the outer and inner regions, we obtain a total gas

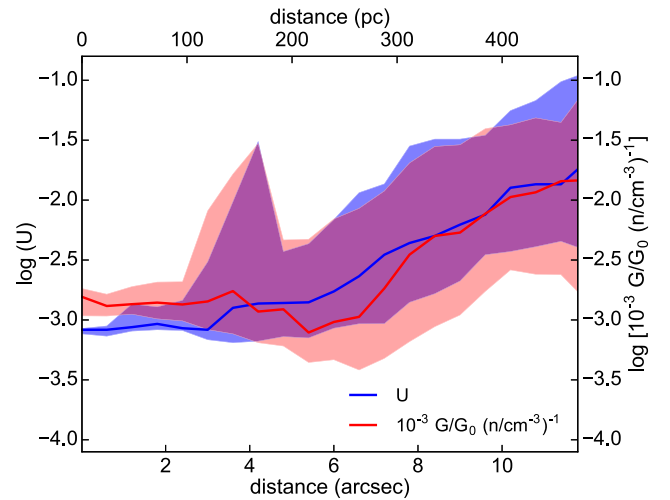


Figure 10. Median radial profile of the He 2-10 ratio between the scaled FUV flux and the density obtained from the maps shown in Fig. 2 (see the text for details). Upper and lower shaded regions denote, respectively, the second and third quartiles. For comparison purposes, we also show the radial profile for the ionization parameter U that follows the same trend.

mass of $1.4 \times 10^8 M_{\odot}$ and $1.9 \times 10^7 M_{\odot}$, respectively, in good agreement with previous estimates.

For what concerns the SFR, we adopt two different approaches. First, by using equation (4), we compute the SFR surface density shown in the right-hand panel of Fig. 5. By summing up the contribution from all spaxels, we obtained $\text{SFR} = 1.2 M_{\odot} \text{ yr}^{-1}$. Secondly, we infer the SFR from the $H\alpha$ map and we correct it for the attenuation through the Calzetti law. For a stellar population with constant SFR over the past 100 Myr, forming stars with an initial mass function consisting of two power laws (slope -1.3 in the range $0.1\text{--}0.5 M_{\odot}$ and slope -2.3 in the range $0.5\text{--}120 M_{\odot}$), Calzetti (2008) reports

$$\text{SFR}(M_{\odot} \text{ yr}^{-1}) = 5.3 \times 10^{-42} L(H\alpha) (\text{erg s}^{-1}), \quad (5)$$

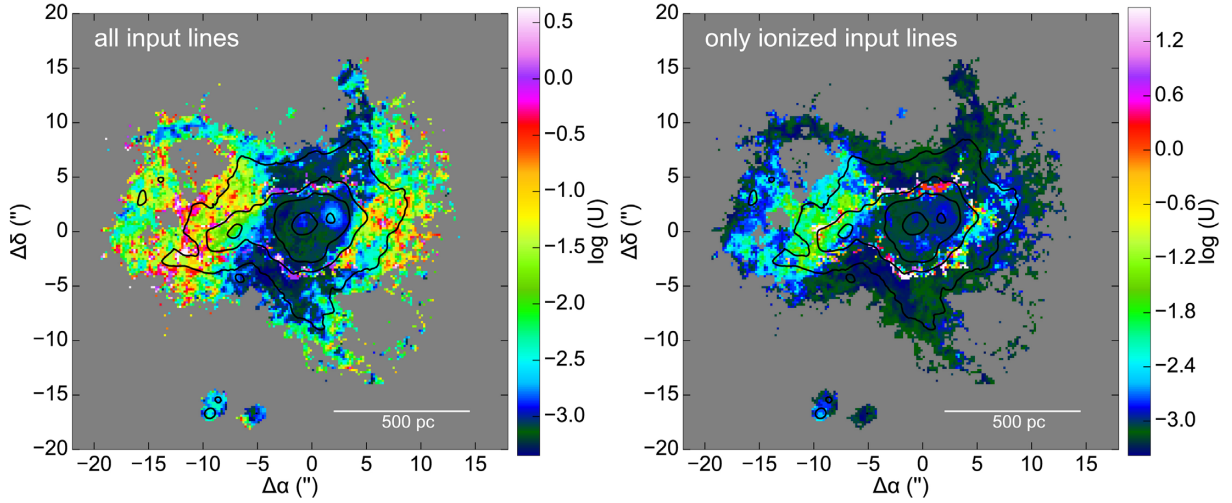


Figure 11. Left-hand panel: map of the ISM ionization parameter (U) inferred for He 2-10 using all the input lines reported in Table 1. Right-hand panel: map of U inferred for He 2-10 using only the ionized input lines reported in Table 1 (i.e. excluding the [O I] and [S II] lines). As in Fig. 1, black lines show the contours of the $H\alpha$ emission line (80, 10, 4, and 1 in units of 10^{-16} erg s $^{-1}$ cm $^{-2}$).

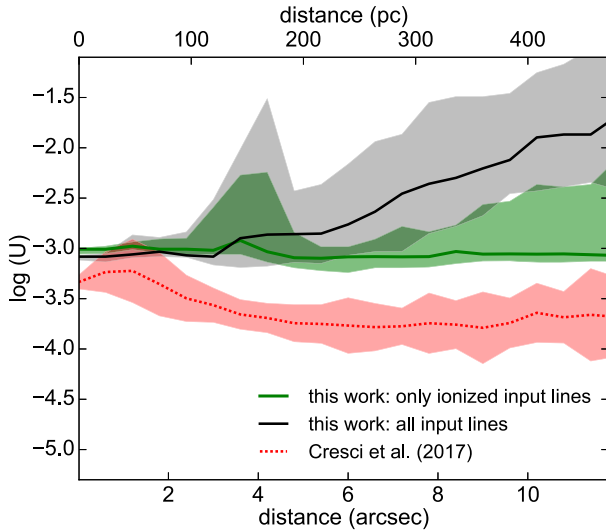


Figure 12. Median radial profiles (median of the inferred physical property values in annular bins of 0.6 arcsec) of the He 2-10 ionization parameter (U) obtained from the maps shown in Fig. 11, centered on $(\Delta\alpha, \Delta\delta) = (0,0)$. Upper and lower shaded regions denote, respectively, the second and third quartiles. We also report the radial profiles as inferred by Cresci et al. (2017).

where $L(H\alpha)$ is the intrinsic luminosity corrected for absorption and interstellar dust attenuation.⁸ Given the fluxes for the $H\alpha$ line and the map of the extinction A_V (see Fig. 2), the uncorrected SFR is $\sim 0.05 M_\odot \text{ yr}^{-1}$. We then corrected the $H\alpha$ fluxes using the Cardelli, Clayton & Mathis (1989) extinction curve (assuming $R_V = 3.1$). By using equation (5) with corrected $H\alpha$ luminosities, and summing up the contribution from the spaxels, we obtained an SFR of $\sim 1.44 M_\odot \text{ yr}^{-1}$. This estimate is consistent with the one by Reines et al. (2011) that, by using the $H\alpha$ (Méndez et al. 1999) and 24 μm (Engelbracht et al. 2005) fluxes, corrected for the Calzetti

⁸Variations of SFR ± 20 per cent for younger/older ages and different metallicities are also possible.

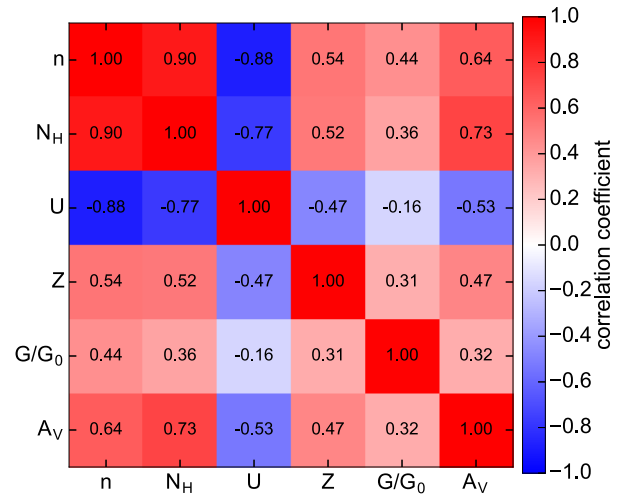


Figure 13. Pearson correlation coefficient C between the value inferred for the physical properties reported in Fig. 2 for He 2-10. There is strong correlation (anticorrelation) for $0.5 < C < 1.0$ ($-1.0 < CC < -0.5$).

(Calzetti et al. 2007) attenuation, found $1.9 M_\odot \text{ yr}^{-1}$. By using the SMC (Prevot et al. 1984; Bouchet et al. 1985; Gordon et al. 2003) extinction curve, we can provide another estimate of the SFR. With the same approach described before, by using our extinction map to correct the $H\alpha$ flux, we obtain: $\text{SFR}_{\text{SMC}} \sim 1.26 M_\odot \text{ yr}^{-1}$. This result underlines the strong dependence of the inferred SFR on the assumed extinction curve.

3.2 Physical correlations

We report in Fig. 13 the Pearson correlation coefficients C between the various physical properties inferred by GAME. Given that the spatial resolution of emission-line fluxes is limited by the seeing (~ 0.68 arcsec; Cresci et al. 2017), in order to have correlation coefficients determinations from independent spaxels, C are computed from 4×4 re-binned maps for the physical properties.

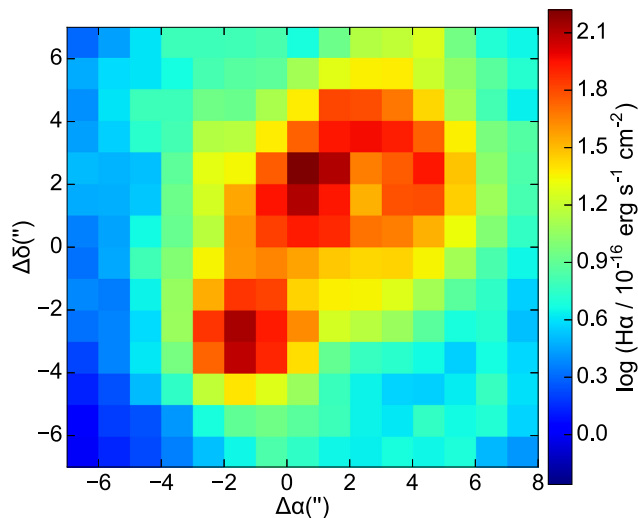


Figure 14. $H\alpha$ image of the galaxy IZw18 (Kehrig et al. 2016) with a scale of $88 \text{ pc arcsec}^{-1}$.

Although determined independently, we find a clear correlation ($C \sim 0.90$) between the density (n) and the column density (N_H). Moreover, the ionization parameter (U) anticorrelates both with the density ($C \sim -0.88$) and the column density ($C \sim -0.77$), due to the dependence of U on the inverse of n . Another expected correlation, such as the one between A_V and N_H is recovered, and we also find $C \sim 0.90$ between A_V and the product $N_H Z$ (see Appendix C).

4 IZW18

Since its discovery (Zwicky 1966), the H II galaxy I Zwicky 18 (hereafter IZw18, also known as Mrk 116, see Fig. 14), is one of the most intriguing blue dwarf galaxies in the local Universe. Zwicky (1966) described it as a system made by two compact galaxies, recognized now as two compact star-forming regions associated with H II regions usually indicated as the NW and SE components (Davidson, Kinman & Friedman 1989). It is located at a distance of 18.2 Mpc (Aloisi et al. 2007) with a corresponding angular scale of $88 \text{ pc arcsec}^{-1}$. It is considered an analogue of high-redshift galaxies (and references therein Leboutteiller et al. 2013) and after the first studies (Sargent & Searle 1970; Searle & Sargent 1972; Searle et al. 1973), it continues to keep attraction thanks to its extremely low metallicity: $Z/Z_\odot \sim 0.026$ (Kunth & Sargent 1986; Pagel et al. 1992; Vílchez & Iglesias-Páramo 1998; Izotov & Thuan 1999; Izotov et al. 1999; Leboutteiller et al. 2013; Kehrig et al. 2016). Since the metallicity is homogeneously distributed (Kehrig et al. 2016), IZw18 should host an underlying old population of intermediate/low-mass stars distributed over the whole area of the galaxy (Vílchez & Iglesias-Páramo 1998), although older/fainter ones are more easily detectable only at the system’s periphery (Contreras Ramos et al. 2011).

4.1 ISM physical properties in IZw18

In this section, we present the ISM physical properties in IZw18 inferred by applying GAME to IFU data taken from Kehrig et al. (2016). IZw18 data were collected by the Potsdam Multi-Aperture Spectrophotometer (PMAS; Roth et al. 2005, 2010) on the 3.5 m telescope at the Calar Alto Observatory. For more details about

Table 2. Emission lines and wavelengths used to analyse the galaxy IZw18. The third column reports the fraction of spaxels with a detected and fitted line (no SNR cuts applied).

Line	Wavelength (Å)	Fraction of spaxels (%)
[O III]	3727	29
[O III]	4363	17
$H\beta$	4861	95
[O III]	5007	98
[O I]	6300	6
$H\alpha$	6563	99
[N II]	6584	13
[S II]	6717	25
[S II]	6731	22

the observations and the data reduction, we refer the reader to Kehrig et al. (2013, 2015, 2016). For IZw18, we have a total of $16 \times 16 = 256$ spectra. By using the input emission lines reported in Table 2, we obtained the maps of the physical properties shown in Figs 15 and 16. A_V , Σ_{SFR} , and Σ_{gas} are computed as in Sections 3.1.3 and 3.1.5, respectively. In the case of IZw18, given the lower number of spaxels available with respect to He 2-10, we did not apply cuts on SNR in our analysis.

The average uncertainties on the physical properties reported in Fig. 15 are $\sigma(x)/x \sim 0.4\text{--}0.6$, where x is the physical property expressed in logarithm. As in the case of He 2-10, we find that the metallicity is the inferred physical property with the lowest uncertainties ($\sigma[\log(Z)] \lesssim 0.1$, corresponding to a relative uncertainty $\sigma(Z)/Z \lesssim 0.3$).

4.1.1 Gas density

In almost all spaxels, we infer density values $\lesssim 10^2 \text{ cm}^{-3}$ (see also Kehrig et al. 2016). The average density is $n \sim 10^{0.7} \text{ cm}^{-3}$. For the column density, we infer an average value of $N_H \sim 10^{21} \text{ cm}^{-2}$, in agreement with van Zee et al. (1998) that report a gas column density exceeding 10^{21} cm^{-2} mainly located in the SE and NW active star-forming regions of IZw18.

4.1.2 Metallicity

In Figs 15 and 17, we show the map and the metallicity distribution, respectively. No significant metallicity gradient is present: the maximum variation among individual spaxels is in fact within a factor of ~ 3 . Although the number of available spaxels is too small for an accurate analysis, this suggests a uniform distribution over spatial scales of hundreds of parsecs (Kehrig et al. 2016). The error-weighted mean metallicity of all spaxels inferred with GAME is $\log(Z/Z_\odot) = -1.32 \pm 0.01$, corresponding to $12 + \log(\text{O}/\text{H}) = 7.37 \pm 0.01$ ($\sim 1/20$ solar).⁹ This result is a factor of 2 larger than the estimate of Kehrig et al. (2016) who found, directly with the electron temperature, $12 + \log(\text{O}/\text{H}) = 7.11 \pm 0.01$ ($\sim 1/40$ solar, see Fig. 17). This mismatch could be due to the discrepancies between different methods (up to ~ 0.15 dex; see Kewley &

⁹Solar gas-phase metallicity is taken to be $12 + \log(\text{O}/\text{H}) = 8.69$ (Allende Prieto, Lambert & Asplund 2001; Asplund et al. 2004), i.e. we assumed the following relation: $\log(Z/Z_\odot) = 12 + \log(\text{O}/\text{H}) - 8.69$.

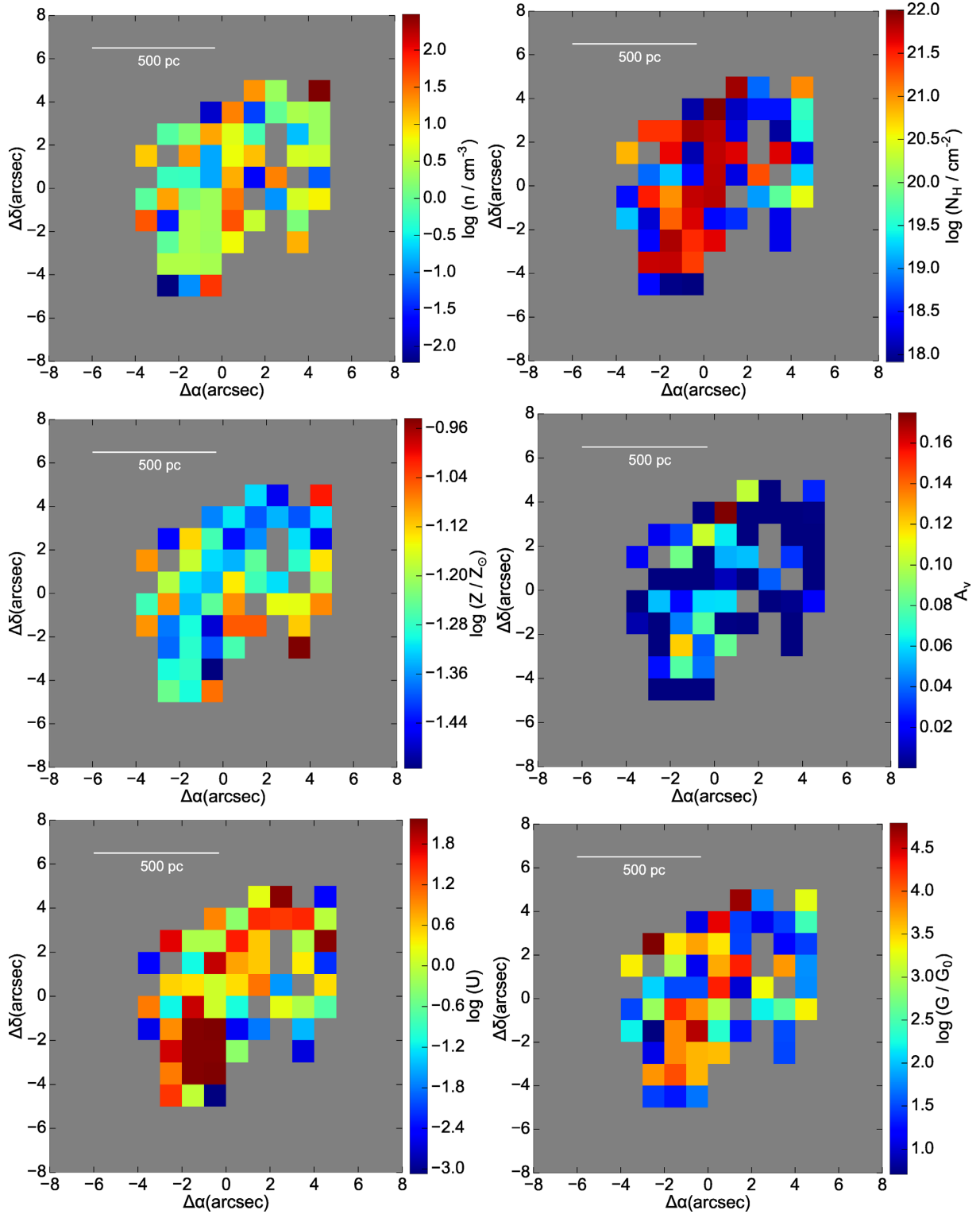


Figure 15. Maps of the ISM physical properties inferred for the galaxy IZw18 using the code GAME (U17; U18): density (n), column density (N_{H}), metallicity (Z), visual extinction (A_V), ionization parameter (U), and the FUV flux in Habing units (G/G_0).

Ellison 2008) or to the well-known difference up to 0.4/0.5 dex between direct methods and techniques based on photoionization models (Stasińska 2002; Kennicutt, Bresolin & Garnett 2003; Garnett, Kennicutt & Bresolin 2004; Kewley & Ellison 2008).

4.1.3 Dust extinction

The map of the visual extinction A_V is reported in Fig. 15. We obtain very low values for the visual extinction ($A_V \lesssim 0.20$) with $A_V \sim 0.01$ mag for the majority of the spaxels.

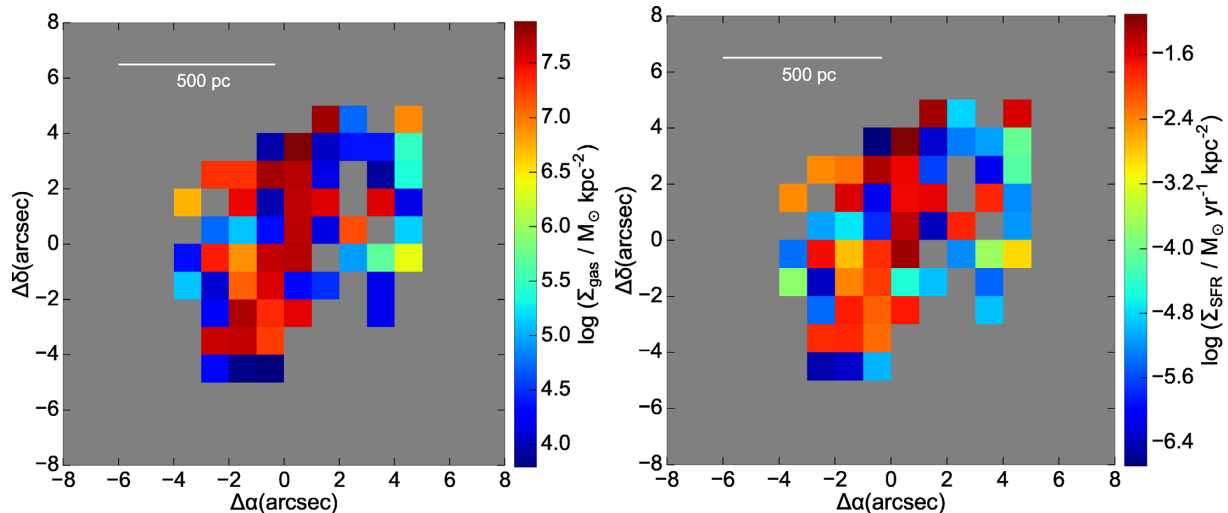


Figure 16. Gas mass surface density (Σ_{gas} , left-hand panel) and star formation surface density (Σ_{SFR} , right-hand panel) for the galaxy IZw18.

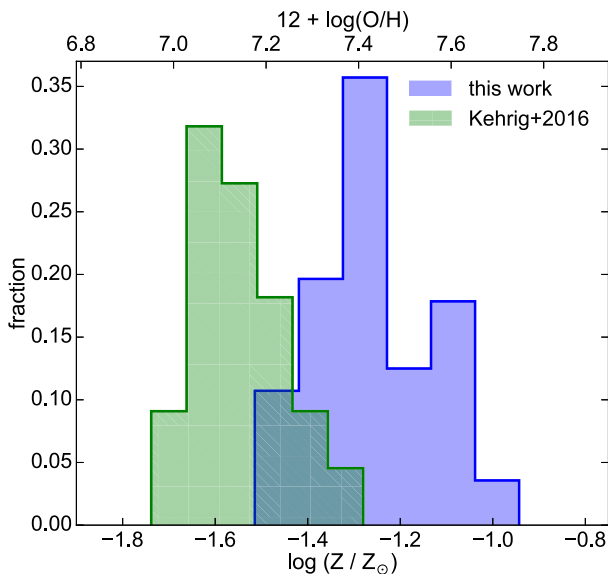


Figure 17. Distribution of metallicity for the spaxels reported in the central left panel of Fig. 15. The blue and green shaded histograms report the results obtained in this work and in Kehrig et al. (2016), respectively.

4.1.4 Interstellar radiation field

Regions with higher ionization parameter are preferentially located in the SE knot where we obtained values as high as $U \sim 10^2$. In the rest of the galaxy, we found $\log(U) \sim 0.5$ – 1 . The most extreme values for U in local analogues of high-redshift galaxies can approach unity (e.g. Bian et al. 2016, 2017; Bian, Kewley & Dopita 2018). In fact, assuming the relation $L(\text{H}\alpha/\text{erg s}^{-1}) = 1.37 \times 10^{-12} Q(H)$ (Osterbrock & Ferland 2006), where $Q(H)$ is the ionizing photon rate in units of s^{-1} , and using the usual definition for U (see footnote 1), we obtain in the SW region $\log(U) \sim -0.5$ – 0.3 (assuming R_S to be 88 pc). However, the GAME output physical property most affected by large uncertainties is the ionization parameter, due to the poorer accuracy in its determination with optical lines only

as input (see also U17, U18). A better constraint of U requires a larger number of emission lines (e.g. fig. D5 in U18), spanning additional wavelength ranges (i.e. UV+optical + IR). Therefore, the extremely high values of U , together with the high G we found could be considered as an additional qualitative indication of the high underlying ionizing flux in this galaxy.

The spatial distribution of G is more uniform across the galaxy, although it is possible to associate higher fluxes in the SE region where $\log(G/G_0) \gtrsim 3.5$. The prominent ionizing flux in the SE knot in our maps, denotes the presence of a clumpy HII component, consisting of numerous knots containing blue stars (Dufour et al. 1996). Such high ionizing fluxes may be originated from the hard SED found in the NW knot, coming from the presence of PopIII stars (see Section 4.2).

4.1.5 Gas mass and SFR surface density

Using the same approach as in Section 3.1.5, we obtain Σ_{gas} and Σ_{SFR} in Fig. 16. Given the lack of reliable determinations of N_H and n in some spaxels (i.e. grey areas in Figs 15 and 16), we can only infer lower limits, $\text{SFR} \gtrsim 0.007 \text{ M}_\odot \text{ yr}^{-1}$, and for the total gas mass $M_{\text{gas}} \gtrsim 6.9 \times 10^6 \text{ M}_\odot$. A previous estimate of $\text{SFR} = 0.1 \text{ M}_\odot \text{ yr}^{-1}$ was obtained by Hunt, Dyer & Thuan (2005), while Aloisi, Tosi & Greggio (1999) provides $\text{SFR} = 6 \times 10^{-2} \text{ M}_\odot \text{ yr}^{-1}$. Legrand (2000) and Legrand et al. (2000), by using a spectrophotometric and chemical model, showed that the photometric properties of IZw18 can be reproduced assuming a continuous SFR as low as $10^{-4} \text{ M}_\odot \text{ yr}^{-1}$ lasting for a Hubble time, with a recent burst of star formation superimposed. Recchi et al. (2004) report an SFR of 4 – $6 \times 10^{-3} \text{ M}_\odot \text{ yr}^{-1}$. These SFR values are required to generate the blue colour of IZw18 (van Zee et al. 1998; Fisher et al. 2014) and the high G and U we found. Galactic winds, produced by stellar winds and SNe could be able to create an outflow and eject part of the ISM. In fact, for such a small galaxy, an SFR of $0.02 \text{ M}_\odot \text{ yr}^{-1}$ can already accelerate the gas and produce the UVB colours, and most of the ionizing luminosity in IZw18 (Martin 1996). The starburst inside this galaxy could also trigger a galactic outflow, with the metals leaving the galaxy far more easily than the unprocessed gas (Mac Low & Ferrara 1999).

4.2 A PopIII-like SED in IZw18 NW?

IZw18 is characterized by an extended nebular He II $\lambda 4686$ emission in its NW component (Kehrig et al. 2015). This implies the presence of a hard ionizing field (i.e. photon energies ≥ 54.4 eV) in this region. This field has been ascribed in the literature (Kehrig et al. 2015, 2016) to the presence of stars with a spectral energy distribution typical of PopIII models (Schaerer 2002; Raiter, Schaerer & Fosbury 2010). In fact, it has been shown (Kehrig et al. 2015) that the He II-ionizing energy budget cannot be explained by conventional excitation sources (i.e. WRs, shocks, X-ray binaries). Vice versa, one of the possible explanations for this emission is the presence of peculiar very hot, ionizing stars that may be (nearly) metal-free (Kehrig et al. 2015, 2016). To further investigate the origin of the He II $\lambda 4686$ emission, we adopt a modified version of GAME that also predicts the intensity of He II $\lambda 4686$ emission line.

In the left-hand panel of Fig. 18, we report the predicted He II $\lambda 4686$ emission-line intensities by considering a reduced library containing only PopII stars (analogous to the ones included in U17). In the central panel is shown the He II $\lambda 4686$ line intensity, obtained by including also PopIII stars (U18). With purely PopII stellar models, it is not possible to obtain emission-line intensities compatible with observations (e.g. fig. 2 of Kehrig et al. 2015): the inferred values are more than one order of magnitude smaller than the observed ones. Adding in the library the contribution from PopIII stars, the He II $\lambda 4686$ intensities can reach values $\gtrsim 10^{-16.0}$ erg s $^{-1}$ cm $^{-2}$, in agreement with observations in the NW region of IZw18. In Fig. 18, we also show the ratio between the PopII and the (PopII + PopIII) contribution to the He II $\lambda 4686$ intensities. We found that there is a negligible contribution from PopII stars in the NW region, where the ratio is $\ll 1$, denoting the possible evidence of a PopIII population. Although there is X-ray emission dominated by a single point source located in the NW region with no significant contribution of faint diffuse emission, the He II emission is essentially due to hot stars (Péquignot 2008; Leboutteiller et al. 2017). Our result suggests that PopII stellar populations cannot account for the observed He II $\lambda 4686$ flux, while PopIII stars, may provide a substantial contribution to the He II emission.

We exploit this result to provide an estimate of the PopII/PopIII relative contribution to the total SFR of IZw18. First, we select the spaxel reported in the right-hand panel of Fig. 18 for which the ratio is approximately 1. Given that in these spaxels no PopIII stars contribution is required to explain the He II emission, we attributed their SFR to PopII stars only. Summing up their contribution, we obtain a value of $\text{SFR}_{\text{PopII}} \sim 0.0031 \text{ M}_{\odot} \text{ yr}^{-1}$. In the remaining spaxels, where the ratio is $\gtrsim 1$, the SFR resulting from the combination of PopII and PopIII bursts is $\sim 0.0039 \text{ M}_{\odot} \text{ yr}^{-1}$. We conclude that PopIII stars could explain at most 52 per cent of the total IZw18 SFR ($\text{SFR}_{\text{PopIII}} \lesssim 0.007 \text{ M}_{\odot} \text{ yr}^{-1}$, see Section 4.1.5).

5 CONCLUSIONS

We presented a comprehensive investigation of the ISM physical properties in two BCGs: the starburst galaxy He 2–10, and the metal-poor dwarf IZw18. This study was possible taking advantage of a Machine Learning (ML) code called GAME (GALaxy Machine learning for Emission lines, see U17, U18), specifically designed to infer the physical properties of multiphase ISM. We applied GAME to MUSE and PMAS IFU observations, obtaining the resolved structure of gas density (n), column density (N_{H}), ionization parameter

(U), metallicity (Z), FUV flux (G), visual extinction (A_{V}), gas mass surface density (Σ_{gas}), SFR surface density (Σ_{SFR}).

GAME proved to be extremely reliable: although each physical property is treated separately and independently (i.e. a different ML model is constructed for each of the physical properties, see U18), the overall morphology of the inferred maps agree with each other and the expected correlations between physical properties such as n with N_{H} (see Fig. 13) hold (see also Appendix C).

Our main conclusions for the galaxy He 2–10 can be summarized as follows.

- (i) It is a star-forming-dominated galaxy with $\text{SFR} \gtrsim 1.2 \text{ M}_{\odot} \text{ yr}^{-1}$, and a total gas mass of $M_{\text{gas}} \sim 1.9 \times 10^7 \text{ M}_{\odot}$.
 - (ii) The ionization parameter in the central regions ($d \lesssim 4$ arcsec) is $U \sim 10^{-3}$, while at larger distances $U \gtrsim 10^{-2}$. The interstellar radiation field in the FUV band G is also strong, with a flat radially median profile and intensities around $G/G_0 \sim 10^{1.5}$, while G reaches its peak in Regions A and B ($G/G_0 \sim 10^3$).
 - (iii) The visual extinction is very high, i.e. $\langle A_{\text{V}} \rangle \gtrsim 3$, with A_{V} in some spaxels exceeding 5–7 mag. These high extinctions are especially found on a region forming a ring around the centre of the galaxy.
 - (iv) The radially median profile for the metallicity is flat with slightly subsolar values [i.e. $\log(Z/Z_{\odot}) \sim -0.2$]. However, the Z distribution inferred in this work covers a quite large range [i.e. $-1.0 \lesssim \log(Z/Z_{\odot}) \lesssim 0.3$] denoting the heterogeneous morphology of He 2–10 in terms of physical properties across its extension.
 - (v) The gas density in Regions A and B reaches values up to $n \sim 10^{3.3} \text{ cm}^{-3}$. Then the radially median profile flattens around a value of $n \sim 1 \text{ cm}^{-3}$. Typical column densities are $N_{\text{H}} \sim 10^{20-10^{22}} \text{ cm}^{-2}$.
- Defining an effective scale height of the disc, as $H = N_{\text{H}}/n$, we obtained $0.3 \lesssim H/\text{pc} \lesssim 30$ in the central region, denoting a relatively small height of the disc. In Regions A and B, we are looking at the typical dimension of GMCs, and we found high values of densities and metallicities, together with high H α and FUV flux G . These evidences suggest that these regions host dense, dusty, and highly star-forming sites.

The main results for IZw18 are the following.

- (i) Summing up the contribution from the analyzed spaxels, we obtained lower limits for the SFR and total gas mass, respectively, of $\text{SFR} \gtrsim 0.007 \text{ M}_{\odot} \text{ yr}^{-1}$ and $M_{\text{gas}} \sim 6.9 \times 10^6 \text{ M}_{\odot}$. The total gas mass of IZw18 has also been estimated by Schneider, Hunt & Valiante (2016) who found $M_{\text{tot}} = M_{\text{H I}} + M_{\text{H}_2} + M_{\text{He II}} = 9.2 \times 10^7 \text{ M}_{\odot}$, with the different phases contributing approximately equal fractions to the total gas mass. A total atomic hydrogen mass of $\sim 10^8 \text{ M}_{\odot}$ has been measured by Lelli et al. (2012) throughout the entire main body, with a radius of ~ 8 arcsec. Both these estimates encompass a region larger than that covered by our spectra; thus our estimate is a lower limit, and consistent with the column densities of $N_{\text{H}} = 2 \times 10^{21} \text{ cm}^{-2}$ found by us and those in H I measured by Lelli et al. (2012) with a 2 arcsec beam. In fact, by integrating the Lelli et al. (2012), H I radial column density distribution up to ~ 4 arcsec (the area covered by our spectral maps), the resulting mass is $8\text{--}30 \times 10^6 \text{ M}_{\odot}$, slightly higher but consistent with our results for a lower limit.
- (ii) The interstellar radiation field is very intense: in the SE knot we obtained very high values for the ionization parameter as high as $U \sim 10^2$, and FUV fluxes $G/G_0 \sim 10^{3.5}$. These high values for U are an additional indication of the underlying high ionizing flux in IZw18, given the large uncertainties associated with the ionization parameter estimates (see U18). The prominent ionizing flux in the

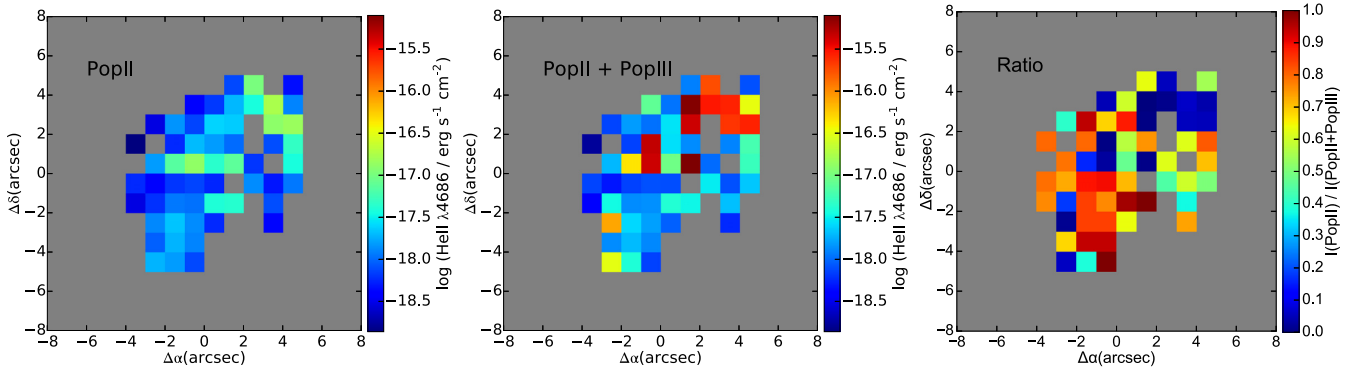


Figure 18. Predicted He II 4686 line emission by GAME for the spaxels of IZw18 using, respectively, the library containing only PopII stars (left-hand panel), and the full library containing also the contribution from PopIII (central panel). Right-hand panel: ratio between the predicted intensities in the left and central panels showing a negligible contribution from PopII stars in the NW region.

SE knot in our maps can be in fact associated with the presence of a clumpy H II component consisting of numerous knots containing blue stars (Dufour et al. 1996).

(iii) We confirmed the extreme poor metal content of IZw18: $\log(Z/Z_{\odot}) = -1.32 \pm 0.01$ [i.e. $12 + \log(\text{O}/\text{H}) = 7.37 \pm 0.01$, corresponding to $\sim 1/20$ solar]. In this galaxy, the metallicity remains also remarkably flat: $-1.5 \lesssim \log(Z/Z_{\odot}) \lesssim -1.0$, with the inferred values being within a factor of 3. These low metallicity correspond also to low visual extinction across the galaxy and low dust-to-gas mass ratios: $A_V \lesssim 0.20$ mag and $\mathcal{D} \sim 10^{-3.5}$, respectively.

(iv) IZw18 presents a low gas density environment, with most of the spaxels having $\log(n/\text{cm}^{-3}) \lesssim 1$. We obtained column densities of $N_H \sim 10^{21} \text{ cm}^{-2}$.

(v) We verified if the extended nebular He II $\lambda 4686$ emission in the NW component of IZw18 found by Kehrig et al. (2015, 2016) could be ascribed to PopIII stars. We implemented a modified version of GAME that is able to predict, in addition to the ISM physical properties, also the value for the intensity of a given emission line (i.e. He II $\lambda 4686$). Then, we compared the predicted He II lines with observations finding that if PopIII stars are not taken into account, the inferred intensities for the He II line are too low compared with observed values. Therefore, PopIII stars may provide a substantial contribution to the He II emission.

ACKNOWLEDGEMENTS

We thank the anonymous referee for her/his careful reading of our manuscript, and for useful comments and suggestions. We thank A. Bolatto for useful discussions and suggestions. AF acknowledges support from the ERC Advanced Grant INTERSTELLAR H2020/740120. GC and LKH are grateful to grant funding from the INAF PRIN-SKA program 1.05.01.88.04. This research was partially supported by the Munich Institute for Astro- and Particle Physics (MIAPP) of the DFG cluster of excellence ‘Origin and Structure of the Universe’.

REFERENCES

Allende Prieto C., Lambert D. L., Asplund M., 2001, *ApJ*, 556, L63
 Allen D. A., Wright A. E., Goss W. M., 1976, *MNRAS*, 177, 91
 Aloisi A., Tosi M., Greggio L., 1999, *AJ*, 118, 302

Aloisi A. et al., 2007, *ApJ*, 667, L151
 Arp H., 1965, *ApJ*, 142, 402
 Asplund M., Grevesse N., Sauval A. J., Allende Prieto C., Kiselman D., 2004, *A&A*, 417, 751
 Baas F., Israel F. P., Koornneef J., 1994, *A&A*, 284, 403
 Bacon R. et al., 2010, in McLean I. S., Ramsay S. K., Takami H., eds, *Proc. SPIE Conf. Ser. Vol. 7735, Ground-based and Airborne Instrumentation for Astronomy III*. SPIE, Bellingham, p. 773508
 Baldwin J. A., Phillips M. M., Terlevich R., 1981, *PASP*, 93, 5
 Bayet E., Gerin M., Phillips T. G., Contursi A., 2004, *A&A*, 427, 45
 Berg D. A. et al., 2012, *ApJ*, 754, 98
 Bian F., Kewley L. J., Dopita M. A., Juneau S., 2016, *ApJ*, 822, 62
 Bian F., Kewley L. J., Dopita M. A., Blanc G. A., 2017, *ApJ*, 834, 51
 Bian F., Kewley L. J., Dopita M. A., 2018, *ApJ*, 859, 175
 Bouchet P., Lequeux J., Maurice E., Prevot L., Prevot-Burnichon M. L., 1985, *A&A*, 149, 330
 Cabanac R. A., Vanzi L., Sauvage M., 2005, *ApJ*, 631, 252
 Calzetti D., 2008, in Knapen J. H., Mahoney T. J., Vazdekis A., eds, *ASP Conf. Ser. Vol. 390, Pathways Through an Eclectic Universe*. Astron. Soc. Pac., San Francisco, p. 121
 Calzetti D. et al., 2007, *ApJ*, 666, 870
 Cardelli J. A., Clayton G. C., Mathis J. S., 1989, *ApJ*, 345, 245
 Conti P. S., 1991, *ApJ*, 377, 115
 Contreras Ramos R. et al., 2011, *ApJ*, 739, 74
 Corbin M. R., Korista K. T., Vacca W. D., 1993, *AJ*, 105, 1313
 Cresci G., Vanzi L., Sauvage M., Santangelo G., van der Werf P., 2010, *A&A*, 520, A82
 Cresci G. et al., 2015, *A&A*, 582, A63
 Cresci G., Vanzi L., Telles E., Lanzuisi G., Brusa M., Mingozzi M., Sauvage M., Johnson K., 2017, *A&A*, 604, A101
 Curti M., Cresci G., Mannucci F., Marconi A., Maiolino R., Esposito S., 2017, *MNRAS*, 465, 1384
 Davidson K., Kinman T. D., Friedman S. D., 1989, *AJ*, 97, 1591
 Dodorico S., Rosa M., Wampler E. J., 1983, *A&AS*, 53, 97
 Dopita M. A., Kewley L. J., Sutherland R. S., Nicholls D. C., 2016, *Ap&SS*, 361, 61
 Dufour R. J., Garnett D. R., Shields G. A., 1988, *ApJ*, 332, 752
 Dufour R. J., Garnett D. R., Skillman E. D., Shields G. A., 1996, in Benvenuti P., Macchetto F. D., Schreier E. J., eds, *Science with the Hubble Space Telescope - II*, Space Telescope Institute (STScI), Baltimore, MD, p. 348
 Engelbracht C. W., Gordon K. D., Rieke G. H., Werner M. W., Dale D. A., Latter W. B., 2005, *ApJ*, 628, L29
 Esteban C., García-Rojas J., Carigi L., Peimbert M., Bresolin F., López-Sánchez A. R., Mesa-Delgado A., 2014, *MNRAS*, 443, 624
 Ferland G. J. et al., 2013, *Rev. Mex. Astron. Astrofis.*, 49, 137

- Fisher D. B. et al., 2014, *Nature*, 505, 186
- Garland C. A., Pisano D. J., Mac Low M.-M., Kreckel K., Rabidoux K., Guzmán R., 2015, *ApJ*, 807, 134
- Garnett D. R., Kennicutt R. C., Jr Bresolin F., 2004, *ApJ*, 607, L21
- Gordon K. D., Clayton G. C., Misselt K. A., Landolt A. U., Wolff M. J., 2003, *ApJ*, 594, 279
- Gorenstein P., 1975, *ApJ*, 198, 95
- Güver T., Özel F., 2009, *MNRAS*, 400, 2050
- Habing H. J., 1968, *Bull. Astron. Inst. Netherlands*, 19, 421
- Haro G., 1956, *Bol. Obs. Tonantzintla Tacubaya*, 2, 8
- Hazard C., 1986, in Kunth D., Thuan T. X., Tran Thanh Van J., Lequeux J., Audouze J., eds, *Astrophysics and Space Science Proceedings, Star-forming Dwarf Galaxies and Related Objects*. Springer-Verlag, Berlin, p. 9
- Hirschauer A. S. et al., 2016, *ApJ*, 822, 108
- Hunt L. K., Dyer K. K., Thuan T. X., 2005, *A&A*, 436, 837
- Izotov Y. I., Thuan T. X., 1999, *ApJ*, 511, 639
- Izotov Y. I., Guseva N. G., Lipovetskii V. A., Kniazev A. I., Stepanian J. A., 1990, *Nature*, 343, 238
- Izotov Y. I., Lipovetsky V. A., Chaffee F. H., Foltz C. B., Guseva N. G., Kniazev A. Y., 1997, *ApJ*, 476, 698
- Izotov Y. I., Chaffee F. H., Foltz C. B., Green R. F., Guseva N. G., Thuan T. X., 1999, *ApJ*, 527, 757
- Izotov Y. I., Thuan T. X., Guseva N. G., 2005, *ApJ*, 632, 210
- Izotov Y. I., Guseva N. G., Fricke K. J., Papaderos P., 2009, *A&A*, 503, 61
- Johnson K. E., Kobulnicky H. A., 2003, *ApJ*, 597, 923
- Johnson K. E., Brogan C. L., Indebetouw R., Testi L., Wilner D. J., Reines A. E., Chen C.-H. R., Vanzil L., 2017, *ApJ*, 853, 125
- Kauffmann G. et al., 2003, *MNRAS*, 346, 1055
- Kawara K., Nishida M., Taniguchi Y., Jugaku J., 1987, *PASP*, 99, 512
- Kawara K., Nishida M., Phillips M. M., 1989, *ApJ*, 337, 230
- Kehrig C. et al., 2013, *MNRAS*, 432, 2731
- Kehrig C., Vílchez J. M., Pérez-Montero E., Iglesias-Páramo J., Brinchmann J., Kunth D., Durret F., Bayo F. M., 2015, *ApJ*, 801, L28
- Kehrig C. et al., 2016, *MNRAS*, 459, 2992
- Kennicutt R. C., Jr, 1998, *ApJ*, 498, 541
- Kennicutt R. C., Jr, Bresolin F., Garnett D. R., 2003, *ApJ*, 591, 801
- Kennicutt R. C., Evans N. J., 2012, *ARA&A*, 50, 531
- Kewley L. J., Dopita M. A., 2002, *ApJS*, 142, 35
- Kewley L. J., Ellison S. L., 2008, *ApJ*, 681, 1183
- Kewley L. J., Dopita M. A., Sutherland R. S., Heisler C. A., Trevena J., 2001, *ApJ*, 556, 121
- Kewley L. J., Groves B., Kauffmann G., Heckman T., 2006, *MNRAS*, 372, 961
- Kobulnicky H. A., Johnson K. E., 1999, *ApJ*, 527, 154
- Kobulnicky H. A., Martin C. L., 2010, *ApJ*, 718, 724
- Kobulnicky H. A., Dickey J. M., Sargent A. I., Hogg D. E., Conti P. S., 1995, *AJ*, 110, 116
- Krumholz M. R., Dekel A., McKee C. F., 2012, *ApJ*, 745, 69
- Kuiper G. P., 1938, *ApJ*, 88, 472
- Kunth D., Sargent W. L. W., 1986, *ApJ*, 300, 496
- Kunth D., Östlin G., 2000, *A&AR*, 10, 1
- Lebouteiller V., Heap S., Hubeny I., Kunth D., 2013, *A&A*, 553, A16
- Lebouteiller V. et al., 2017, *A&A*, 602, A45
- Legrand F., 2000, *A&A*, 354, 504
- Legrand F., Kunth D., Roy J.-R., Mas-Hesse J. M., Walsh J. R., 2000, *A&A*, 355, 891
- Lelli F., Verheijen M., Fraternali F., Sancisi R., 2012, *A&A*, 537, A72
- Lequeux J., Peimbert M., Rayo J. F., Serrano A., Torres-Peimbert S., 1979, *A&A*, 80, 155
- Mac Low M.-M., Ferrara A., 1999, *ApJ*, 513, 142
- McQuinn K. B. W. et al., 2015, *ApJ*, 812, 158
- Marconi A., Risaliti G., Gilli R., Hunt L. K., Maiolino R., Salvati M., 2004, *MNRAS*, 351, 169
- Markarian B. E., 1967, *Astrofizika*, 3, 24
- Martín-Hernández N. L., Schaerer D., Peeters E., Tielens A. G. G. M., Sauvage M., 2006, *A&A*, 455, 853
- Martin C. L., 1996, *ApJ*, 465, 680
- Meier D. S., Turner J. L., Crosthwaite L. P., Beck S. C., 2001, *AJ*, 121, 740
- Melnick J., Terlevich R., Eggleton P. P., 1985, *MNRAS*, 216, 255
- Méndez D. I., Esteban C., Filipović M. D., Ehle M., Habert F., Pietsch W., Haynes R. F., 1999, *A&A*, 349, 801
- Nguyen D. D., Seth A. C., Reines A. E., den Brok M., Sand D., McLeod B., 2014, *ApJ*, 794, 34
- Osterbrock D. E., Ferland G. J., 2006, *Astrophysics of Gaseous Nebulae and Active Galactic Nuclei*. University Science Books, Sausalito, CA
- Pagel B. E. J., Simonson E. A., Terlevich R. J., Edmunds M. G., 1992, *MNRAS*, 255, 325
- Péquignot D., 2008, *A&A*, 478, 371
- Predehl P., Schmitt J. H. M. M., 1995, *A&A*, 293, 889
- Prevot M. L., Lequeux J., Prevot L., Maurice E., Rocca-Volmerange B., 1984, *A&A*, 132, 389
- Pustilnik S. A., Kniazev A. Y., Pramskij A. G., 2005, *A&A*, 443, 91
- Raiter A., Schaerer D., Fosbury R. A. E., 2010, *A&A*, 523, A64
- Recchi S., Matteucci F., D'Ercole A., Tosi M., 2004, *A&A*, 426, 37
- Reina C., Tarengi M., 1973, *A&A*, 26, 257
- Reines A. E., Deller A. T., 2012, *ApJ*, 750, L24
- Reines A. E., Sivakoff G. R., Johnson K. E., Brogan C. L., 2011, *Nature*, 470, 66
- Reines A. E., Reynolds M. T., Miller J. M., Sivakoff G. R., Greene J. E., Hickox R. C., Johnson K. E., 2016, *ApJ*, 830, L35
- Roth M. M. et al., 2005, *PASP*, 117, 620
- Roth M. M. et al., 2010, in Holland A. D., Dorn D. A., eds, *Proc. SPIE Conf. Ser. Vol. 7742, High Energy, Optical, and Infrared Detectors for Astronomy IV*. SPIE, Bellingham, p. 774209
- Salaris M., Cassisi S., 2005, *Evolution of Stars and Stellar Populations*. Wiley, New York
- Sánchez S. F. et al., 2017, *MNRAS*, 469, 2121
- Santangelo G., Testi L., Gregorini L., Leurini S., Vanzil L., Walmsley C. M., Wilner D. J., 2009, *A&A*, 501, 495
- Sargent W. L. W., Searle L., 1970, *ApJ*, 162, L155
- Schaerer D., 2002, *A&A*, 382, 28
- Schmidt M., 1959, *ApJ*, 129, 243
- Schneider R., Hunt L., Valiante R., 2016, *MNRAS*, 457, 1842
- Searle L., Sargent W. L. W., 1972, *ApJ*, 173, 25
- Searle L., Sargent W. L. W., Bagnuolo W. G., 1973, *ApJ*, 179, 427
- Skillman E. D., Kennicutt R. C., Jr, 1993, *ApJ*, 411, 655
- Skillman E. D. et al., 2013, *AJ*, 146, 3
- Stasińska G., 2002, *Rev. Mex. Astron. Astrofis. Ser. Conf.*, 12, 62
- Terlevich R., Melnick J., Masegosa J., Moles M., Copetti M. V. F., 1991, *A&AS*, 91, 285
- Tolstoy E., Hill V., Tosi M., 2009, *ARA&A*, 47, 371
- Tully R. B. et al., 2013, *AJ*, 146, 86
- Ucci G., Ferrara A., Gallerani S., Pallottini A., 2017, *MNRAS*, 465, 1144
- Ucci G., Ferrara A., Pallottini A., Gallerani S., 2018, *MNRAS*, 477, 1484
- Vacca W. D., Conti P. S., 1992, *ApJ*, 401, 543
- Vacca W. D., Johnson K. E., Conti P. S., 2002, *AJ*, 123, 772
- van Zee L., Westpfahl D., Haynes M. P., Salzer J. J., 1998, *AJ*, 115, 1000
- Vanzil L., Rieke G. H., 1997, *ApJ*, 479, 694
- Vanzil L., Combes F., Rubio M., Kunth D., 2009, *A&A*, 496, 677
- Vasudevan R. V., Fabian A. C., 2009, *MNRAS*, 392, 1124
- Vílchez J. M., Iglesias-Páramo J., 1998, *ApJ*, 508, 248
- Watson D., 2011, *A&A*, 533, A16
- Zhu H., Tian W., Li A., Zhang M., 2017, *MNRAS*, 471, 3494
- Zwicky F., 1965, *ApJ*, 142, 1293
- Zwicky F., 1966, *ApJ*, 143, 192

APPENDIX A: PHOTON FLUX IN HE 2-10 IS STAR-FORMING DOMINATED

In order to investigate the nature of the dominant radiation source, it is possible to use the Baldwin, Phillips & Terlevich (BPT) diagram (Baldwin, Phillips & Terlevich 1981), used to distinguish between star-forming regions and active

galactic nuclei. The analysis in this section closely follows the one presented in Cresci et al. (2017, i.e. their fig. 5), but here we also show the applicability of GAME to He 2-10 and with slightly different arguments how the stellar component dominates the radiation field in the galaxy. The BPT diagram makes use of two pairs of lines close in wavelength in order to minimize the effects of dust and continuum subtraction uncertainties. The line ratios involved in the BPT diagram are usually the [N II]/H α ratio, primarily sensitive¹⁰ to the shape of the ionizing spectrum just above 1 Rydberg, and the [O III]/H β ratio that probes the 1-3 Rydberg range.

The BPT diagram for the models within the GAME library (U18) and the spaxels in He 2-10 are, respectively, shown in the upper and lower left panels in Fig. A1. Here, we report three zones (Kewley et al. 2001; Kauffmann et al. 2003; Kewley et al. 2006): (a) regions dominated by star formation, (b) intermediate regions, (c) AGNs. Star-forming regions are below the Kauffmann et al. (2003) line (black solid line in Fig. A1):

$$\log([\text{O III}]/\text{H}\beta) = \frac{0.61}{\log([\text{N II}]/\text{H}\alpha) - 0.05} + 1.3. \quad (\text{A1})$$

Intermediate regions fall between this and the Kewley et al. (2001) line (dashed line in Fig. A1):

$$\log([\text{O III}]/\text{H}\beta) = \frac{0.61}{\log([\text{N II}]/\text{H}\alpha) - 0.47} + 1.19. \quad (\text{A2})$$

Regions dominated by AGN contribution are above the two lines. In the right-hand panel of Fig. A1, we marked these three zones with different colours. The map results to be dominated by green dots (i.e. more than 95 per cent of spaxels), meaning that almost all the line emitting gas is ionized by young stars. This result confirms the assumption that the models contained within the library used by GAME (i.e. photoionization models coming only from stars without X-ray sources or AGNs, U18) can be applied to this galaxy.

In order to further validate this result, we started from the radiation energy density of the stars contained within the galaxy, assumed to be a uniformly emitting sphere of radius r :

$$u = \frac{L_*}{4\pi r^2 c}, \quad (\text{A3})$$

where $L_* = \varepsilon M_*$ is the luminosity produced by the stars inside the galaxy, M_* is the total stellar mass contained in the galaxy, and ε the conversion between the stellar mass itself and the luminosity ($L_\odot M_\odot^{-1}$). By considering the previous estimates for the stellar mass contained in He 2–10 $M_* = 10^9 M_\odot$ (Reines et al. 2011; Nguyen et al. 2014) and a conservative value based on the mass–luminosity relation for a subsolar mass of $\varepsilon = 0.1 L_\odot M_\odot^{-1}$ (Kuiper 1938; Salaris & Cassisi 2005), we obtained $L_* = 10^8 L_\odot$. We further computed the distance d at which the radiation energy density of the stars is equal to that produced by the X-ray source by simply imposing:

$$\frac{L_X}{4\pi d^2 c} = \frac{L_*}{4\pi R^2 c}, \quad (\text{A4})$$

where L_X is the luminosity of the X-ray source and R is the radius of the uniformly emitting sphere, that we assumed to be $R = 6 \text{ arcsec} = 240 \text{ pc}$, based on the effective radius of the inner component of the galaxy provided by Nguyen et al. (2014). Given the recent estimate of $L_X \approx 10^{38} \text{ erg s}^{-1}$ of Reines et al. (2016), we obtain that $d \sim 4 \text{ pc}$. Of course, more realistic values (i.e. greater values) for ε due to young massive stars and the application of bolometric corrections (Marconi et al. 2004) for L_X up to ~ 10 (e.g. Vasudevan & Fabian 2009) mean that the distance d could remain the same or become even smaller (if one assumes $\varepsilon \sim 1$). The region where the energy density of the X source is relevant is very small compared to the effective radius of the galaxy. The galaxy radiation field is therefore completely dominated by the stellar component. This confirms both the results by Cresci et al. (2017) and guaranteeing the applicability of GAME to this source.

¹⁰The BPT lines are also sensitive to the ionization parameter, N and O abundances, and density- versus ionization-bounded H II regions.

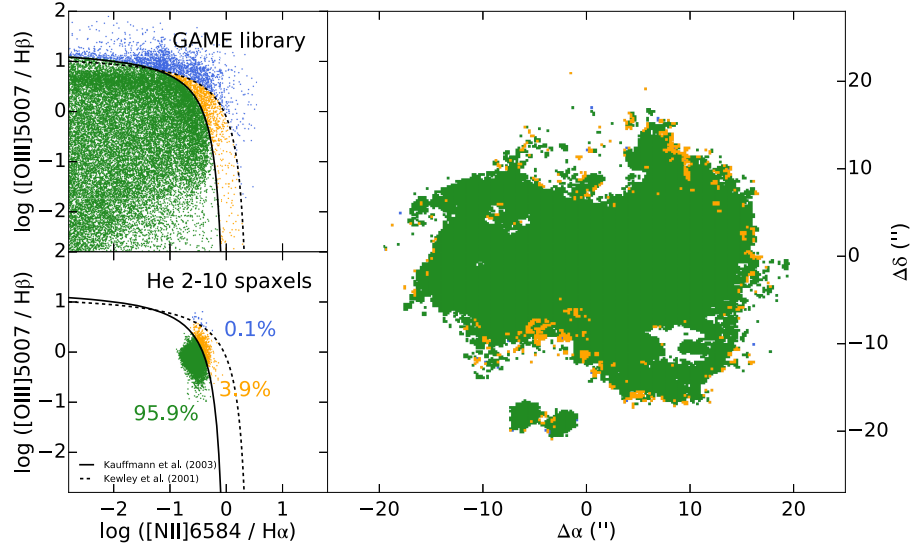


Figure A1. Upper left panel: BPT diagram for the models contained within the library of synthetic models of GAME. As expected, because the assumed input spectra are stellar, nearly all the models fall within the star-forming region. Lower left panel: BPT diagram for the observed spaxels of He 2-10 where we also added the percentages of the different region in the observed line ratios. Right-hand panel: map for He 2-10 colour-coded based on the BPT diagram. In green are reported the spaxels having line ratios below the line reported in Kauffmann et al. (2003) denoting regions dominated by star formation.

APPENDIX B: MAPS OF UNCERTAINTIES FOR HE 2-10

GAME determines 10 000 different values of each physical property (U18). The associated uncertainties are given by the standard deviations of these 10 000 realizations.

Fig. B1 shows the relative uncertainties on the He 2-10 physical properties derived directly by game and reported in Fig. 2.

The typical uncertainties in the central region of the galaxy (within ~ 10 arcsec from the centre) are smaller than 30 per cent, while in the case of the metallicity the vast majority of spaxels have lower uncertainties even at larger distances. The highest uncertainties remains associated to the ionization parameter U , although in the central part of the galaxy, $\sigma[\log(U)]/\log(U)$ reduces to values $\lesssim 10$ per cent.

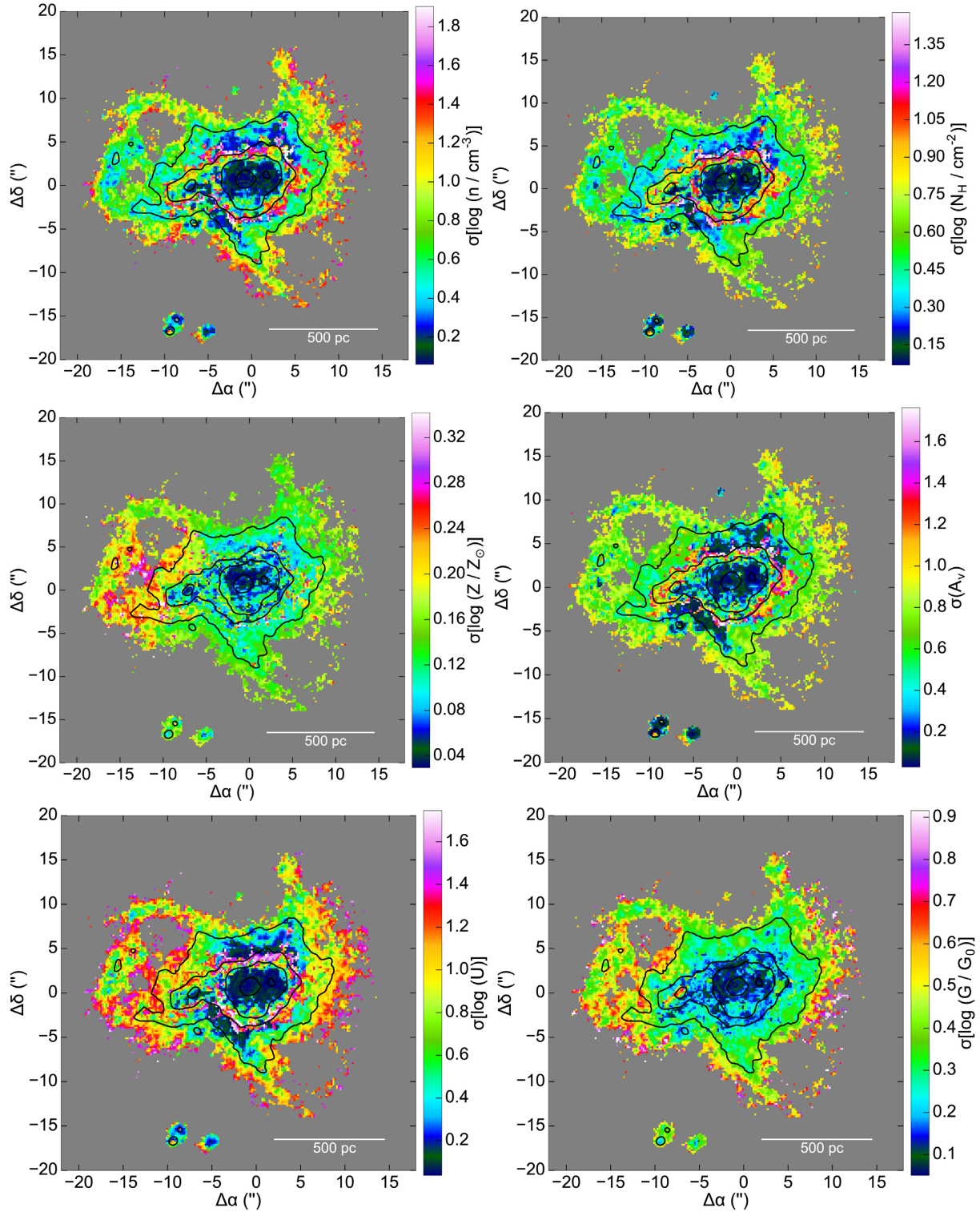


Figure B1. Relative uncertainties on the He 2-10 ISM physical properties reported in Fig. 2: density (n), column density (N_{H}), metallicity (Z), visual extinction (A_V), ionization parameter (U), and the FUV flux in the Habing band (G/G_0). As in Fig. 1, black lines show the contours of the $\text{H}\alpha$ emission (80, 10, 4, and 1 in units of $10^{-16} \text{ erg s}^{-1} \text{ cm}^{-2}$). In the upper left corner, we report the average relative uncertainty on the inferred values.

APPENDIX C: GAS-TO-EXTINCTION RATIO

In this section, as an additional check of consistency for GAME, we also study the recovered gas-to-extinction ratio inside the two galaxies.

In the Galaxy, the extinction in the optical band (A_V) and the hydrogen column density (N_{H}) are related by the following expression (Reina & Tarenghi 1973; Gorenstein 1975; Predehl & Schmitt 1995; Güver & Özel 2009; Watson 2011; Zhu et al.

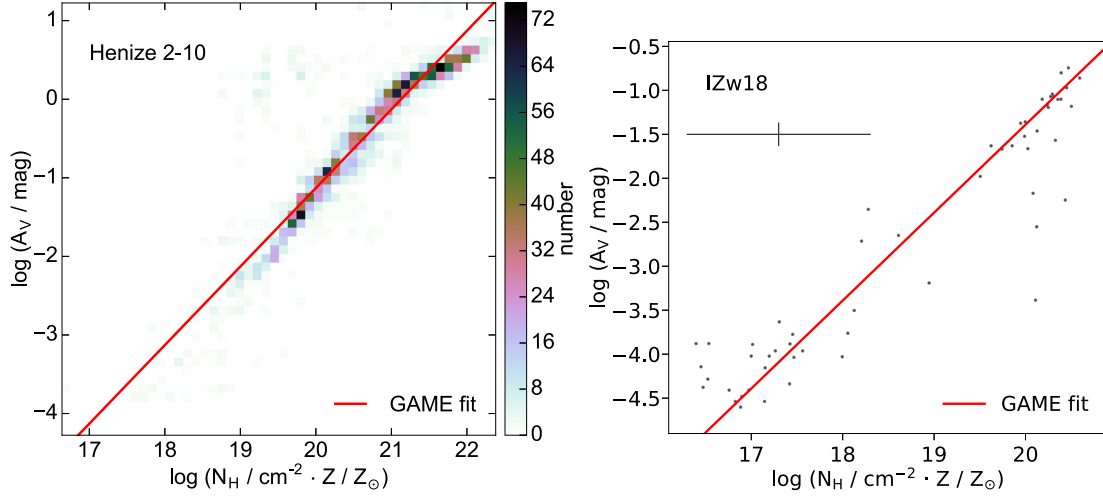


Figure C1. Left-hand panel: 2d histogram for the visual extinction A_V as a function of the product $N_H Z$ for all the analyzed spaxels in He 2-10. The vast majority of points are located around the line. Right-hand panel: visual extinction A_V as a function of the product $N_H Z$ for the analyzed spaxels in IZw18. Red lines denote the fit to the data using equation (C2). The upper-left cross denotes the typical error bar on the points.

2017):

$$A_V = \frac{N_H}{\alpha_{MW}} \approx \frac{N_H}{2.21 \times 10^{21} \text{ cm}^{-2}} \text{ mag}, \quad (\text{C1})$$

where α_{MW} is the Milky Way hydrogen-to-extinction ratio. In the GAME library, we assumed instead the following functional form:

$$A_V = \frac{1}{\alpha} N_H Z, \quad (\text{C2})$$

where $\alpha = 2.52 \times 10^{21} \text{ cm}^{-2} \text{ mag}^{-1}$. To assess the GAME performances, we use our results on A_V , N_H , and Z inferred by

GAME (discussed in Sections 3 and 4). The red lines in Fig. C1, represent the best fit of equation (C2) to the GAME results. For He 2-10 and IZw18, we find $\alpha_{\text{He2-10}} = (2.40 \pm 0.02) \times 10^{21} \text{ cm}^{-2} \text{ mag}^{-1}$ and $\alpha_{\text{IZw18}} = 2.46_{-0.37}^{+0.43} \times 10^{21} \text{ cm}^{-2} \text{ mag}^{-1}$, respectively. The α coefficients are compatible, implying that GAME is able to recover in a consistent way internal relations within the library in spite of the fact that the physical properties are recovered independently.

This paper has been typeset from a \LaTeX file prepared by the author.